

JGR Planets

RESEARCH ARTICLE

10.1029/2021JE006993

Key Points:

- Guadalupe-Matarranya fan in the Ebro Basin, Spain, is a large fluvial fan with fluvial ridges similar to fans on Mars
- Fluvial ridges are exhumed channel belts from rivers 1.4 m deep, with sediment-transport intermittency factor of 0.004 (range: 0.0004–0.04)
- If martian depositional rivers had similar intermittency, some persisted at least millions of years

Supporting Information:

Supporting Information may be found in the online version of this article.

Correspondence to:

M. P. Lamb,
mpl@caltech.edu

Citation:

Hayden, A. T., Lamb, M. P., Myrow, P. M., Mohrig, D., Williams, R. M. E., Cuevas Martínez, J. L., et al. (2021). The Oligocene-Miocene Guadalupe-Matarranya fan, Spain, as an analog for long-lived, ridge-bearing megafans on Mars. *Journal of Geophysical Research: Planets*, 126, e2021JE006993. <https://doi.org/10.1029/2021JE006993>

Received 16 JUL 2021
Accepted 3 NOV 2021

The Oligocene-Miocene Guadalupe-Matarranya Fan, Spain, as an Analog for Long-Lived, Ridge-Bearing Megafans on Mars

A. T. Hayden^{1,2} , M. P. Lamb¹ , P. M. Myrow³, D. Mohrig⁴ , R. M. E. Williams⁵ , J. L. Cuevas Martínez⁶, B. T. Cardenas^{4,1} , C. P. Findlay^{7,8} , R. C. Ewing⁷ , and B. J. McElroy⁹ 

¹Division of Geological and Planetary Sciences, California Institute of Technology, Pasadena, CA, USA, ²Now at California Council on Science and Technology, Sacramento, CA, USA, ³Geology Department, Colorado College, Colorado Springs, CO, USA, ⁴Department of Geological Sciences, The University of Texas at Austin, Austin, TX, USA, ⁵Planetary Science Institute, Tucson, AZ, USA, ⁶Departament de Dinàmica de la Terra i de l'Oceà, Facultat de Ciències de la Terra, Universitat de Barcelona, Barcelona, Spain, ⁷Department of Geology and Geophysics, Texas A&M University, College Station, TX, USA, ⁸Now at Chevron Corporation, Houston, TX, USA, ⁹Department of Geology and Geophysics, University of Wyoming, Laramie, WY, USA

Abstract Numerous sedimentary fans on Mars have been studied to better understand the early martian hydrological system. Of particular interest is to estimate the duration of fluvial activity from alluvial fan size by dividing deposit volume by bankfull sediment flux. However, such a calculation requires an intermittency factor—a parameter relating sediment discharge from channel-filling (bankfull) floods to the long-term mean sediment discharge—which is poorly constrained. Here, we investigated fluvial fan deposits from the Oligocene–Miocene Caspe Formation, Spain, as an analog to fans on Mars because it has exhumed channel belts that create sinuous ridges in the modern topography, similar to those observed on Mars that are used for paleohydraulics. We made measurements of the thicknesses of dune and bar cross sets within exhumed channel belts at nine field sites to reconstruct bankfull channel depth (~1.4 m) and bankfull sediment flux (~0.48 m³/s). We estimated total bed-material sediment volume of the fan (362 km³) from stratigraphic thickness, the area containing exhumed channel belts, porosity and sand fraction. Combined with previous constraints on depositional timespan (~6 Myr), we calculated a sediment-transport intermittency factor of 0.004 (range: 0.0004–0.04). Our approach can be applied to Mars by using remote sensing measurements of fluvial ridge morphology, which indicates the possibility of long depositional timespans exceeding millions of years for martian fans.

Plain Language Summary We examined Oligocene-Miocene river deposits in the Guadalupe-Matarranya fan (Ebro Basin, Spain) as an analog for river deposits on Mars that potentially represent long durations of river activity. Similar to deposits on Mars, the Guadalupe-Matarranya fan has been differentially eroded creating networks of branching, sinuous ridges that represent former river channel belts. Based on measurements of river bar and dune deposits, we estimated that the ancient rivers were sand-bedded and 1.4 m deep and that they carried a bankfull sediment discharge of 0.48 m³/s. Using these data, we calculated that the entire fan could have been built in as little as 24,000 years if there was continuous bankfull flow in the rivers. However, in reality, the fan was built over 6 million years, highlighting the vast amount of time that sediment transport was inactive. Applying a similar fraction of intermittent sediment transport to case studies on Mars suggests that martian river systems could have been intermittently persistent for millions of years.

1. Introduction

A central goal of Mars science is to understand whether early Mars had a long-lived, stable hydrological cycle or multiple intermittent, short-lived, river-forming episodes (e.g., Pollack et al., 1987; Segura et al., 2002; Wordsworth et al., 2018). Morphological and sedimentological evidence of ancient rivers and lakes are evidence of prior surface water on Mars (e.g., Craddock & Howard, 2002; Goudge et al., 2015; Moore et al., 2003), but it is unknown whether surface water persisted over significant timescales (e.g., Palumbo et al., 2020). For instance, many deposits are thought to have formed in less than 10⁶ years of fluvial activity (e.g., Jezero Delta; Lapôtre & Ielpi, 2020). Other work suggests active river systems occurred in at least two distinct episodes during the Noachian and Early Hesperian (Baker & Partridge, 1986; Howard et al., 2005), a total duration exceeding 10⁸ years. Evidence that river systems persisted over a significant fraction of those episodes would support the

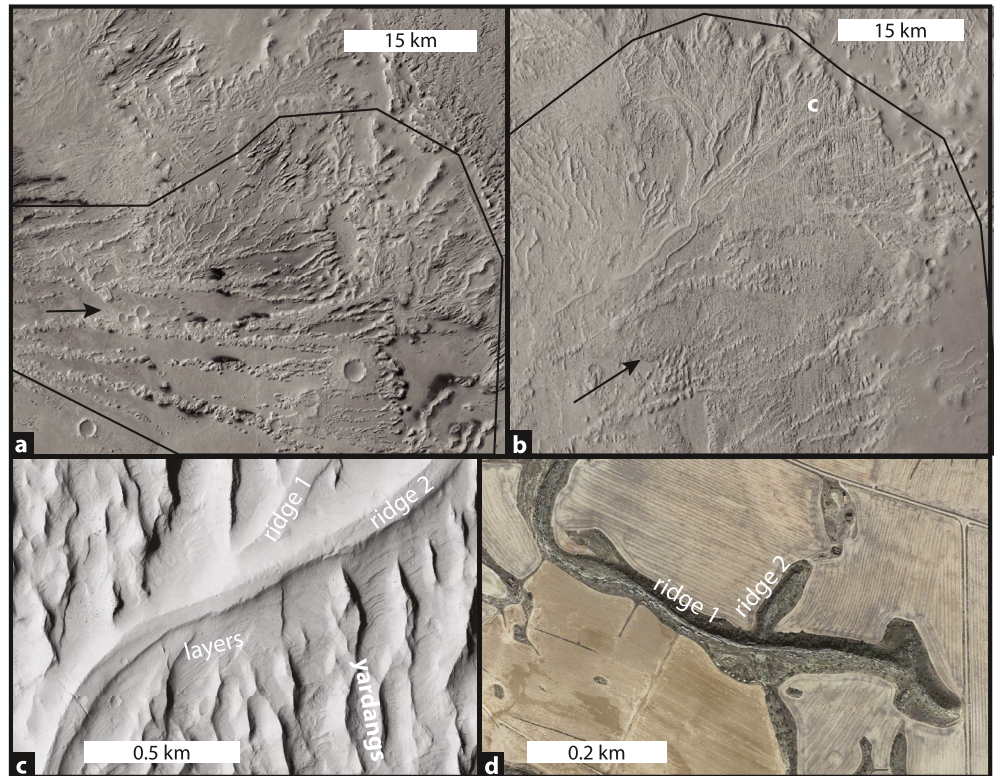


Figure 1. Examples of sinuous ridges in megafans from the Aeolis Dorsa region of Mars (a–c) and the Ebro Basin of Spain (d). (a and b) CTX images of portions of two large branching ridge networks in Aeolis Dorsa (area = 2100 and 2700 km²; 155.0°E, 5.0°S; 151.0°E, 6.5°S); black polygon traces the rough outline of the megafan, and black arrow indicates inferred paleoflow direction. White “c” in (b) indicates location of (c). (c) HiRISE image (PSP_002279_1735) of the ridges in the network of (b), zoomed in on sinuous ridges crossing with aeolian yardangs. The material under the ridge caprock shows layering. (d) Crossing vegetated bedrock ridges at our Field Site 9, surrounded by farmland.

hypothesis of long-lived clement climates, whereas total depositional timespans of hundreds to thousands of years would support the hypothesis of short-lived clement climates driven by rare events (Halevy & Head, 2014; Palumbo et al., 2018).

On Earth, the longest records of river activity are contained within thick successions of fluvial strata (e.g., Johnson et al., 1985; Klausen et al., 2014). On Mars, a number of large and potentially thick alluvial fans have been identified; for example, particularly striking and well-studied branching networks of sinuous ridges occur in several fans at Aeolis Dorsa (e.g., Figures 1a and 1b; Lefort et al., 2012, 2015; DiBiase et al., 2013; Kite, Howard, Lucas, Armstrong, et al., 2015). Sinuous ridges are common on martian fans and represent channel or channel-belt deposits that have been exhumed by the wind via differential erosion (Burr et al., 2009, 2010; Hayden et al., 2019; Pain et al., 2007). Thus, branching ridge networks might represent deposits from bifurcating rivers or stacked fan lobes due to river avulsion, both of which are common on alluvial fans or deltas (e.g., DiBiase et al., 2013; Kite et al., 2013; Lefort et al., 2015). The size and depositional character of fans in Aeolis Dorsa resemble terrestrial megafans, which exceed 10³ km² area, are deposited by low-gradient (<0.1°) depositional rivers, and represent important sediment sinks over long geologic timescales (Latrubesse, 2015; Leier et al., 2005). The timespan of fluvial activity on some martian megafans has been estimated to exceed 10⁶ years in some cases (e.g., Hoke et al., 2011; Kite et al., 2013) and even up to 10⁸ years (e.g., Orofino et al., 2018), but uncertainty in these calculations is large.

Estimates for the timespan of fluvial activity, $\sum t$, are often based on mass balance, where the fan sediment volume, V , is divided by the product of the volumetric bankfull sediment discharge, $Q_{s,bf}$, and an intermittency factor, I_f (e.g., Kleinhans, 2005; Morgan et al., 2014);

$$\sum t = V / (Q_{s,bf} I_f) \quad (1)$$

$Q_{s,bf}$ is the sediment transport that occurs during a flood event that fills the channel to its brim, and it can be estimated for ancient systems from reconstructions of channel geometry (Schumm, 1972) from observations of channel sedimentology or fluvial ridge morphology (Allen, 1963; Hayden et al., 2019; Mohrig et al., 2000). Rivers can experience a range of flow conditions, including long periods of time in which sediment is not transported. To account for this variability, the intermittency factor is used to correct for the total amount of sediment that was transported relative to what would have been transported with continuous bankfull flow (i.e., $I_f = V / (Q_{s,bf} \sum t)$; Equation 1; Paola et al., 1992). Therefore, $I_f = 1$ indicates continuous bankfull flow, and decreasing $I_f < 1$ indicates more intermittent sediment transport and longer depositional timespan.

Equation 1 has been used to calculate depositional timespans for a number of fan deposits on Mars (e.g., Kleinhans et al., 2010; Morgan et al., 2014), but these timespans are uncertain because the intermittency factor is poorly constrained. Although fluvial ridges have been identified across Earth (Zaki et al., 2021), studies have yet to reconstruct the intermittency factor from observations of ridge-bearing terrestrial fans.

In this work, we present observations from the Oligocene-Miocene Guadalope-Matarranya fan in the Caspe Formation, Spain. The Guadalope-Matarranya fan is an ideal field site to test the time-reconstruction methods of Equation 1 because it has abundant exposures of channel belts that can be used to reconstruct paleochannel dimensions (e.g., Cabrera, 1983; Cuevas Martínez et al., 2007, 2010; Mohrig et al., 2000), and there are constraints on the total depositional timespan from magnetostratigraphy (e.g., Barbera et al., 1994, 2001; Garcés et al., 2008; Valero et al., 2014). Furthermore the exhumed channel belts resemble sinuous ridges on Mars, enabling comparison of calculations based on remote-sensing measurements versus in-situ sedimentological measurements. We measured sedimentary structures and ridge geometries (Section 3) to constrain the paleo-hydraulics of the system and estimate the intermittency factor (Section 4), and discuss the implications of our results for Mars science (Section 5).

2. Field Area

We studied the Guadalope-Matarranya fan, which is a large fluvial fan deposit in the Oligocene-Miocene Caspe Formation in the Ebro Basin, Spain (Figure 2). Modern exposure of the Guadalope-Matarranya fan covers ~3000 km² in the south end of the Ebro Basin (Cabrera, 1983). The Ebro Basin was endorheic throughout the deposition of the Guadalope-Matarranya fan, and all sediment was trapped locally. Deposition occurred in an arid to semi-arid climate (Cabrera & Sáez, 1987). The Ebro River began draining the Ebro Basin through the Catalan Coastal Range sometime between 12 and 7.5 Ma (García-Castellanos & Larrasoña, 2015), and it has now exposed at least 400 m of stratigraphy of the Caspe Formation (Cuevas Martínez et al., 2007, 2010; Mohrig et al., 2000). The partially exposed Puig Moreno anticline runs east-west through the center of the fan, and reported tectonic dip magnitudes are less than 5° in a direction away from the anticline (Figure 2c).

The Guadalope-Matarranya fan consists of channel-belt deposits made of sandstone and conglomerate (estimated at 2%–25% of the volume; Cuevas Martínez et al., 2010) encased in floodplain deposits comprising mudstone and sandstone sheets (Cabrera et al., 1985; Cuevas Martínez et al., 2010; Friend et al., 1979). Channel belts range from 1 to 15 m thick and are up to 90 m wide, with width-to-thickness ratios averaging 6 with standard deviation of 2 (Cabrera et al., 1985; Cuevas Martínez et al., 2010). The most common sedimentary structures in the channel belts are bar-scale cross-beds, interpreted to represent downstream-migrating alternate bars, and laterally accreting bank-attached bars based on whether their accretion directions are more parallel or perpendicular, respectively, to the accretion direction of paleoflow indicators like dune cross-sets (Cuevas Martínez et al., 2007; Friend et al., 1986; González-Bonarino et al., 2010; Mohrig et al., 2000). Many channel bodies are amalgamations of distinct generations of fluvial deposits, some of which are separated by thin mudstone drapes. Evidence for depositional hiatuses also include bioturbation and erosional surfaces in the floodplain material that indicate gaps between periods of fluvial activity (Cuevas Martínez et al., 2007, 2010; Mohrig et al., 2000). Mohrig et al. (2000) found that most channel belts represent a single generation of bar lateral accretion, although 24% of channel belts showed evidence of multiple stacked accretion sets separated by low angle erosion surfaces (i.e., multiple stories).

Channel-belt paleo-hydraulic indicators vary little across the field area. Flow-depth estimates from bar set thicknesses range from 1 to 3.3 m, with a mean of 1.4 m, and are similar in a given channel body and across the fan system (Mohrig et al., 2000). Observed changes from south to north include: single-story bodies become more

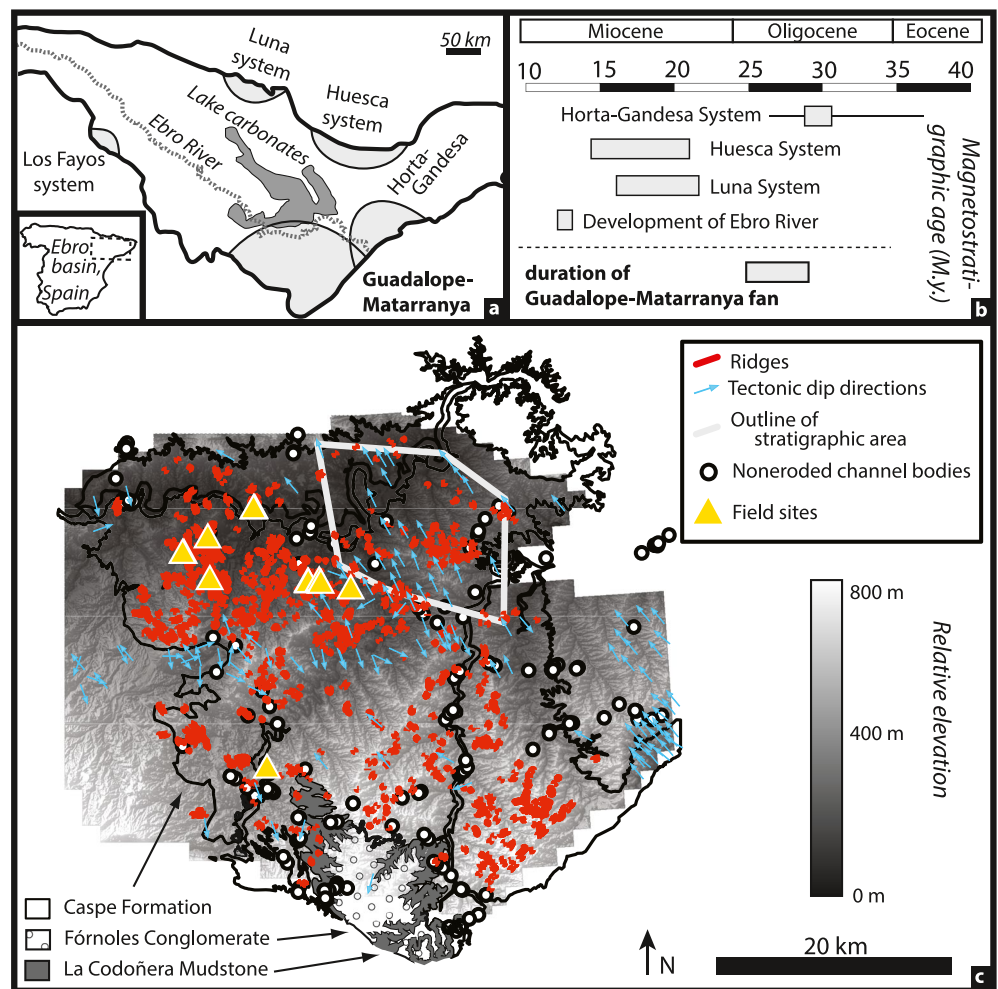


Figure 2. Field area. (a) Overview of Guadalupe-Matarranya fan within the Ebro Basin, along with other Oligocene–Miocene fluvial fan systems and the modern Ebro River. (b) Magnetostratigraphic data for different fan systems in the Ebro Basin. Horta–Gandesa system dates are from Jones et al. (2004), Swanson-Hysell and Barbeau (2007, 2008), and Garcés et al. (2008) [box represents overlap of dates; line represents uncertainty between studies]. Guadalupe-Matarranya dates are taken from the Caspé Formation, which spans 30–24 Ma (Garcés et al., 2008; Valero et al., 2014). (c) Shaded elevation map (0.5 m/px) of area bearing ridges (red lines). The Guadalupe-Matarranya fan comprises the Caspé Formation (black outline), Fórnoles Conglomerate, and La Codoñera Mudstone (Cabrera, 1983). White outline is the area used for the stratigraphic model, determined from the convex hull of an area where tectonic dips are aligned.

common, grain size decreases, and paleocurrent directions diverge, indicating a distributary geometry (Allen et al., 1983; Cabrera et al., 1985, 2002; Cuevas Martínez et al., 2007; Mohrig et al., 2000).

The southeastern part of the Guadalupe-Matarranya fan where it interfingers with the Gandesa–Horta fan has been dated through magnetostratigraphy (Gandesa/Bot sections of Barberá et al., 2001; Jones et al., 2004; Valero et al., 2014). Although the resulting dates have been the subject of debate due to conflicting stratigraphic correlations (Garcés et al., 2008; Swanson-Hysell, 2007, 2008), most interpretations, including the most recent (Valero et al., 2014), show a minimum depositional timespan of ~4 Myr. Our best estimate for deposition duration is 6 Myr, from 30 to 24 Ma, which we derived using the bounds on alluvial facies in the Mina Pilar–Mequinenza and Bot sections (Garcés et al., 2008; Valero et al., 2014); this estimate is similar to the timespan reported by Mohrig et al. (2000) based on the earlier work of Barberá et al. (1994).

Sinuuous ridges resembling those observed on Mars (e.g., Burr et al., 2009; Dickson et al., 2021) are abundant across the Guadalupe-Matarranya fan (Figure 2; Cuevas Martínez et al., 2007; Friend et al., 1979; Riba et al., 1967). Many of the ridges were mapped in prior studies (e.g., Cuevas Martínez et al., 2007). Ridges are

typically 100–1000 m long, although many multi-km-length ridges exist (Cuevas Martínez et al., 2010; Mohrig et al., 2000; Williams, 1975). Ridge intersections are common, and exhibit both Y- and X-shaped geometries in planview, indicating channel belts that converge or diverge (Y shapes) or cross (X shapes) at different stratigraphic levels (Cuevas Martínez et al., 2010).

3. Methods

3.1. Field Methods

The main goals of our fieldwork in the Ebro Basin were to understand the origin of the ridges that resemble ridges on Mars, collect sedimentological data to constrain the bankfull channel characteristics, estimate the total volume of the fan, and finally combine the measurements to calculate the intermittency factor. We visually mapped 883 ridges across the field area (Figure 2c) using a lidar digital elevation model (DEM) (0.5 m/px; downloaded from the Instituto Geográfico Nacional, www.ign.es/) that we processed in order to highlight the steep slopes of ridge caprocks. We then extracted 2388 elevation transects, spaced 50 meters apart, perpendicular to the manually traced centerlines of 237 ridges selected randomly across the field area. Following the methods of Hayden et al. (2019), we used the transects to characterize caprock width, caprock thickness, and ridge relief by manually identifying the caprock edges (as the base of an uppermost, near-vertical unit) and the bottom of the sloping flanks (at the transition to a nearly flat section). Measurements were corrected for the reported tectonic dips of 2° toward 345° (Beltrán Cabrera et al., 1981; van den Hurk et al., 1997; Navarro Juli et al., 1994; Hernandez Samaniego et al., 2004; Costa Mercadal et al., 1997) in part of the study area (Figure 2c) by adding to the DEM a plane that has equal-magnitude dip in the opposite direction.

Nine specific locations were selected for detailed fieldwork on the basis of ridge prominence in air photos, and observed ridge branching and crossing patterns, all of which allowed us to reconstruct channel-belt bifurcations and stratigraphic stacking patterns. We mapped the field sites with a DJI Phantom 4 quadcopter, and used the images in Agisoft Metashape to create a high-resolution DEM and orthophoto using photogrammetry to aid further analysis of stratigraphy (see figures in the Supporting Information).

To reconstruct bankfull channel geometries and sediment discharge, we recorded sedimentary structures and median grain size following the methodology of Hayden et al. (2019). Median grain size was identified visually with a grain-size card. Sedimentary structures of interest include cross-stratification, such as those produced by ripples, dunes, and bar clinofolds. We measured preserved ripple cross-strata, exposed in cross-section and in a few cases on the tops of caprocks, with thicknesses of millimeter to centimeter scale (Allen, 1963). Dune cross-beds of decimeter thickness are exposed in cross section (Figure 3; Allen, 1963), and we also observed dune trough cross-lamination in planview along ridge tops (i.e., rib-and-furrow structures; Figure 3b; Stokes, 1953). Although clinofolds (Figure 3d) in our field area resemble larger (meter-scale; Allen, 1963) dune cross-strata, they were interpreted as bar strata based on superimposed smaller-scale dune cross sets with differing paleo-current directions, or by S-shaped sets that “roll over” at the top, indicating a fully preserved bar structure (Hajek & Heller, 2012; Mohrig et al., 2000). Bar structures are also exposed in plan-view on ridge tops as quasi-planar inclined beds over decameter scales (Figure 3b). We compared accretion directions of the bar strata to paleo-channel banks inferred from scour surfaces bounding channel bodies to determine if the bars were downstream migrating or laterally migrating.

We included in our analysis previously unpublished data on the geometry of channel-belt sandstone bodies from a prior field excursion to the same area (Mohrig et al., 2000, Figure 2). This dataset includes 118 sandstone bodies with 5–95 percentile intervals of 4.6–100 m for width (median = 13 m), 0.4–9.7 m for thickness (median = 3.5 m), and 1.4–10.3 (median = 4.5) for breadth-thickness ratios.

3.2. Reconstructing Paleochannel Depth

We reconstructed paleochannel depth from data collected from fluvial deposits and ridges (Allen, 1963; Bhat-tacharya et al., 2016; Cardenas et al., 2020; Hayden et al., 2019; Hayden & Lamb, 2020; Mohrig et al., 2000; Williams et al., 2009). Bar clinofold thickness (t_{bar}) was assumed to approximate the flow depth at bankfull (H_{bf}) (Allen, 1965; Hajek & Heller, 2012; Mohrig et al., 2000), that is,



Figure 3. Examples of observed sedimentary structures. (a) Stacked, truncated cross-bed sets. Hammer in the center of image is 30 cm tall. (b) Rib-and-furrow structures, in this case migrating along a linear bank-attached bar (see Figure 5a for location). Yellow tape measure (20 cm long) for scale. (c) Climbing dune cross-stratification, outlined by white lines. Hammer is 30 cm tall. (d) Truncated bar clinoforms (white lines).

$$H_{bf} = t_{bar} \quad (2)$$

Truncated bar strata yield a minimum depth by Equation 2.

Thickness of dune cross-stratification (t_{dune}) is also used to interpret flow depths, but there is higher uncertainty in this metric than in Equation 2 because there is a distribution of dune heights present for a given flow depth (Bradley & Venditti, 2017), and a distribution of truncated dune cross-bed set thicknesses for a given dune height (Paola & Borgman, 1991). Combining the small-river ($H_{bf} < 2.5$ m, consistent with flow-depth reconstructions from bar heights) relationship between dune height and flow depth from Bradley and Venditti (2017, Table 7) with the relationship between dune height and dune set thickness (t_{dune}) of Paola and Borgman (1991), as presented by Leclair and Bridge (2001), yields

$$H_{bf}/t_{dune} = 10.2 \left(\text{bounds: } 6.6 - 35 \right) \quad (3)$$

Paleohydrologic techniques also have been developed for use with remote-sensing observations of fluvial ridges (e.g., Goudge et al., 2018; Hayden et al., 2019; Hayden & Lamb, 2020). Hayden et al. (2019) found that thickness of a ridge caprock (T) serves as a proxy for bankfull depth

$$T/H_{bf} = 1.5 \left(\text{bounds: } 1 - 4 \right) \quad (4)$$

Their compilation of the geometry of modern and ancient channel belts includes data from the Ebro Basin (Mohrig et al., 2000), as well as other sites. Equation 4 supports the idea that rivers tend to avulse to a new location after aggrading ~ 1 to 4 times channel depth due to gravitational instability (Ganti et al., 2014; Mohrig et al., 2000; Slingerland & Smith, 2004), and that erosion during ridge formation leaves caprock thickness relatively unmodified (Hayden et al., 2019; Hayden & Lamb, 2020).

3.3. Calculating Sediment Discharge

Estimates of bankfull channel depth (H_{bf}) and median grainsize (D_{50}) were used to calculate bankfull sediment discharge ($Q_{s,bf}$). Note the *bf* subscript, which indicates when the parameter is intended to only apply to bankfull conditions. We estimated bankfull volumetric sediment discharge of the bed-material load (bed load plus suspended bed material) using the model from Engelund and Hansen (1967) for sand-bedded rivers because it is simple and remains among the most accurate predictors across a broad range of flow conditions (Petkovsek, 2019). Non-dimensional sediment discharge per unit width (q_t^*) is related to the friction factor (C_f) and Shields stress (τ_*) by

$$q_t^* = (0.05/C_f)(\tau_*)^{5/2} \quad (5)$$

where $q_t^* = Q_s/W(RgD_{50}^3)^{0.5}$, W is flow width, R is the submerged specific density of the sediment (1.65 for quartz in water), g is gravitational acceleration, and τ_* is the nondimensional Shields stress.

The friction factor is defined as $C_f = (gHS)/U^2$ for steady and uniform flow, where H is flow depth, S is the bed slope and U is the depth-averaged flow velocity. We used the Engelund and Hansen (1967) relationship for sand-bedded rivers to calculate depth-averaged flow velocity:

$$U/u_{*s} = (1/\kappa)\ln[11H_s/k_s] \quad (6)$$

where u_{*s} is the component of shear velocity due to skin friction (i.e., the friction due to grain roughness; $u_{*s} = \sqrt{gH_sS}$, assuming normal flow), $\kappa = 0.41$ is von Karmán's constant, k_s is a bed roughness height, and H_s is the flow depth related to skin friction (Einstein, 1950). The roughness height relevant for skin friction is:

$$k_s = n_k D_{50} \quad (7)$$

where n_k is about 2.5 for many rivers (Engelund & Hansen, 1967). To account for the effect of drag from bedforms (dunes and bars), Engelund and Hansen (1967) related the skin friction component of nondimensional shear stress, τ_{*s} , to the total nondimensional shear stress, τ_* , by:

$$\begin{aligned} \tau_{*s} &= 0.06 + 0.4\tau_*^2 \quad \text{for } \tau_{*s} \leq \tau_* \\ \tau_{*s} &= \tau_* \quad \text{otherwise} \end{aligned} \quad (8)$$

in which,

$$\begin{aligned} \tau_* &= HS/RD_{50} \\ \tau_{*s} &= H_sS/RD_{50} \end{aligned} \quad (9)$$

for steady and uniform flow. To constrain the bed slope, we combined Equation 9 with the empirical relationship of Trampus et al. (2014), who found

$$\tau_{*,bf} = 17Re_p^{-0.5} \quad (10)$$

where $Re_p = \sqrt{RgD_{50}}D_{50}/\nu$ and ν is the kinematic viscosity of water. To solve for C_f , we first solved for H_s by combining Equations 8–10, combined H_s with Equations 6 and 7 to solve for U , solved for S with Equations 9 and 10, then used the definition of $C_f = (gHS)/U^2$.

Bankfull channel width of single-thread rivers is linearly related to bankfull depth (e.g., Parker et al., 2007), so we used the median value of the bankfull ratio of width to depth from a large compilation (Trampus et al., 2014):

$$W_{bf}/H_{bf} = 18 \quad (11)$$

To calculate bankfull sediment discharge from inputs of grain size and bankfull depth, we calculated width using Equation 11, calculated shear stress under the assumption of steady and uniform flow using Equation 9, and used the calculated C_f as described above.

3.4. Measuring Deposit Volume

Equation 1 requires an estimate of the total volume of sediment transported by bankfull sediment discharge. Most sediment-discharge calculations, including Equation 5, exclude washload—generally the mud fraction in sand-bedded rivers (e.g., Einstein & Chien, 1953). Thus, for the Ebro basin, we calculated the total volume of deposited sand and gravel as

$$V = AFf(1 - \lambda) \quad (12)$$

in which A is the deposit area in planview, F is the thickness of fluvial stratigraphy, f is the fraction of the deposit composed of sandstone and conglomerate, and λ is porosity. The thickness was assumed to be constant across the area, which has a maximum error of a factor of three if the deposit is cone-shaped rather than having a constant thickness. This approach followed Hayden, Lamb, and McElroy et al. (2021) but differs from other applications of Equation 1 that assumed washload was not incorporated into the deposit (e.g., Kleinhans, 2005; Kleinhans et al., 2010).

We used the previously mapped area, $A = 3000 \text{ km}^2$, of the Guadalupe-Matarranya fan (Figure 2c), which includes the Caspe Formation, the Fórnoles Conglomerate, and La Codoñera mudstones (Cabrera, 1983). To measure stratigraphic thickness, we used the part of the mapped ridge area with greatest areal extent of consistent tectonic dips (Figure 2c). The base of the section corresponds with the position of the Matarranya River, which indicates additional section is likely below this lower bound. The top of the section was defined at the cliff-forming, lacustrine carbonate beds of the Los Monegros Formation at the north end of the field area. We measured a stratigraphic thickness of 700 m as the vertical distance between the bounds with the tectonic tilt-removed DEM. We estimated $f = 0.25$ using the upper bound on the coarse-sediment fraction for the Guadalupe-Matarranya fan (Cuevas Martínez et al., 2010). Porosity was taken to be $\lambda = 0.31$ by combining the fraction of modern porosity (13%) and the fraction of post-depositional matrix material (18%), both measured in a Caspe Formation sandstone from near Alcañiz (Buj & Gisbert, 2010). Both f and λ are unlikely to vary significantly, and $\lambda = 0.30\text{--}0.35$ has been in common use with Equation 1 (e.g., Kleinhans et al., 2010; Morgan et al., 2014). A value of $f = 0.25$ is expected because terrestrial fluvial basins are typically 20%–80% sand (Heller et al., 2015), and f values on the lower end of this range are expected when narrow channel belts are observed, such as the fluvial ridges and ribbon sandstone bodies in our study areas; higher f values would instead be associated with broader amalgamated sandstone sheets.

3.5. Intermittency Factor and Uncertainty

We calculated the intermittency factor using Equation 1, where bankfull sediment discharge was calculated from Equation 5, the bed-material sediment volume (362 km^3 , which excludes pore space and mudstone) was found from Equation 12, and the timespan of fluvial activity was estimated to be 6 Myr (Section 2).

To quantify uncertainty in our calculation of intermittency factor, we assumed that all contributing uncertainties are independent and distributed log-normally, and we combined them with Gaussian error propagation. The main source of uncertainty on intermittency factor is the bankfull sediment discharge, which we quantified by assessing each of the terms in the calculation ($Q_{s,bf} \sim W_{bf} \tau_{*,bf}^{5/2} C_f^{-1/2}$). We constrained the uncertainty on each term as the 5–95 percentile bounds of the ratio between predicted and measured values in the Trampus et al. (2014) compilation of over 500 rivers at bankfull conditions, finding uncertainty in width (Equation 11), shear stress (Equation 10), and friction factor (Equations 6–10) as factors of 2.5, 5, and 2, respectively, around the central estimate. Bankfull geometry reconstructions from Equations 3 and 4 have an uncertainty of a factor of 2, which we combined into the error estimate because bankfull width scales directly with depth (Equation 11). Based on these factors, we estimated the uncertainty on bankfull sediment discharge to be a factor of ~ 9 . Combining this with bed-material-sediment volume and duration, we estimated an uncertainty for the intermittency factor (from Equation 1) to be a factor of ~ 10 around the central estimate (total factor of 100 from 5 to 95 percentile bounds). The unknown number of simultaneously active channels is incorporated into the value of I_f rather than the uncertainty.

4. Results

4.1. Field Observations

We investigated 883 ridges using DEMs, and visited nine sites for detailed analysis. From the 883 ridges, we found that ridges are typically 100–800 m long, and the longest is 3 km. Ridges cover 3000 km²—almost the entire exposed Caspe Formation—but appear less common or absent in the parts of the Guadalupe-Matarranya fan that are mapped as Fórnoles Conglomerate or La Codoñera Mudstone (Figure 2c). We observed that ridges with axes parallel to the topographic strike tend to be longer than those that are parallel to the topographic dip. Sinuosity (ridge length divided by straight-line distance between endpoints) ranged from 1.0 to 3.0, with shorter ridges generally having a wider distribution of sinuosity values because they sample only a fraction of the ridge. The stratigraphic thickness of the digital stratigraphic model is 0.7 km. Ridge caprocks form cliffs that are visible in the DEM, and the 5–95 percentile ranges in breadth, thickness, and relief are 10–50, 0.5–4.4, and 0.3–11 m, respectively. There are no significant trends across the field area in parameters measured from remote sensing.

Site 4 is a typical example of ridges observed in our field sites (Figure 4); the other eight sites are all similar, and comparable analyses are provided in the Supporting Information. Site 4 has five ridges that intersect each other and stand 2–26 m above the surrounding plain (Figures 4a and 4b), which includes the highest-relief ridges we studied. Ridges are composed of a sandstone caprock atop mudstone with thin sandstone interbeds (Figure 4c). Caprock breadths are 6–40 m and thicknesses are 0.3–4.8 m (Figure 4d). Sandstone talus blocks up to several meters in diameter line the ridge flanks and are absent in the surrounding plains. The tilt-corrected digital elevation model and UAV photo shows that Ridges 1 and 3 and the Plateau occur at different stratigraphic levels (Figures 4a and 4b), and field observations of erosional surfaces separating caprock sandstone units indicate each ridge is stratigraphically distinct (e.g., Figures 5a and 5b).

Caprocks at Site 4 are made of fine to medium sandstone, and most contain abundant cross-strata. We observed 55 truncated sets of cross strata 0.05–0.80 m thick (means of 0.13–0.20 m for each caprock) which we interpreted as dune cross sets on the basis of their size and trough cross-bedding. We also measured 15 rib-and-furrow structures on ridge tops and found dune accretion directions within 20° of the main ridge axis (Figure 4b). Larger bar clinoforms have accretion directions ranging from parallel to perpendicular to the dune accretion directions (Figure 4b). In plan-view, there is one example of a long (20+ m) inclined planar bar set with interbedded smaller rib-and-furrow structures, indicating superimposed dunes (Figures 3b and 5a). The bar set has an accretion direction perpendicular to the paleo-flow, as indicated by the rib-and-furrow structures, which suggests that it is a bank-attached point bar deposit.

Caprocks unconformably overlie mudstone, with some laterally extensive, thin sandstone sheets interspersed. We examined in detail one of the ridges at Site 4 with 26 m of mudstone exposed (Figure 4c). We found 9 tabular beds of fine sandstone, 0.1–1.4 m thick, with internal structures including burrows and planar lamination. Several layers within the mudstone contain carbonate nodules.

Site 4 has five ridge junctions, all between Ridge 1 and another ridge, which we examined in the field and in the high-resolution stratigraphic model to see if they represent channel or channel-belt bifurcations, or if they represent superposition of sandstone bodies at distinct stratigraphic levels. Ridge 1 is stratigraphically above the Plateau and below Ridge 3 and has distinct paleoflow directions from the other two (Figure 4b), so we interpret all three as distinct. Ridge 2 is at the same vertical position as Ridge 1, but a major erosional surface separates the two (Figure 5a) and their paleo-flow directions are different (Figure 4b) so we interpret them as representing distinct stratigraphic intervals. Ridges 4 and 5 are eroded at their intersection with Ridge 1; however, there are channel bodies visible in outcrop that align with the caprocks of Ridges 4 and 5 (Figure 5b), so we interpret the caprocks as having been continuous with the channel bodies prior to erosion. The channel bodies interpreted as remnants of Ridges 4 and 5 are below and separated from the caprock of Ridge 1 by erosional surfaces (Figure 5b), so we interpret these ridges to also be distinct channel bodies at different stratigraphic levels. We were able to detect the vertical offsets between Ridges 1 and 3 and the Plateau based on cliff shadows in the UAV imagery and their 3D position in the DEM. In contrast, Ridges 1, 2, 4, and 5 were at similar elevations in the DEM and lacked clear cross-cutting relationships in the UAV imagery, and therefore, appear at indistinguishable stratigraphic position using remote-sensing datasets alone.

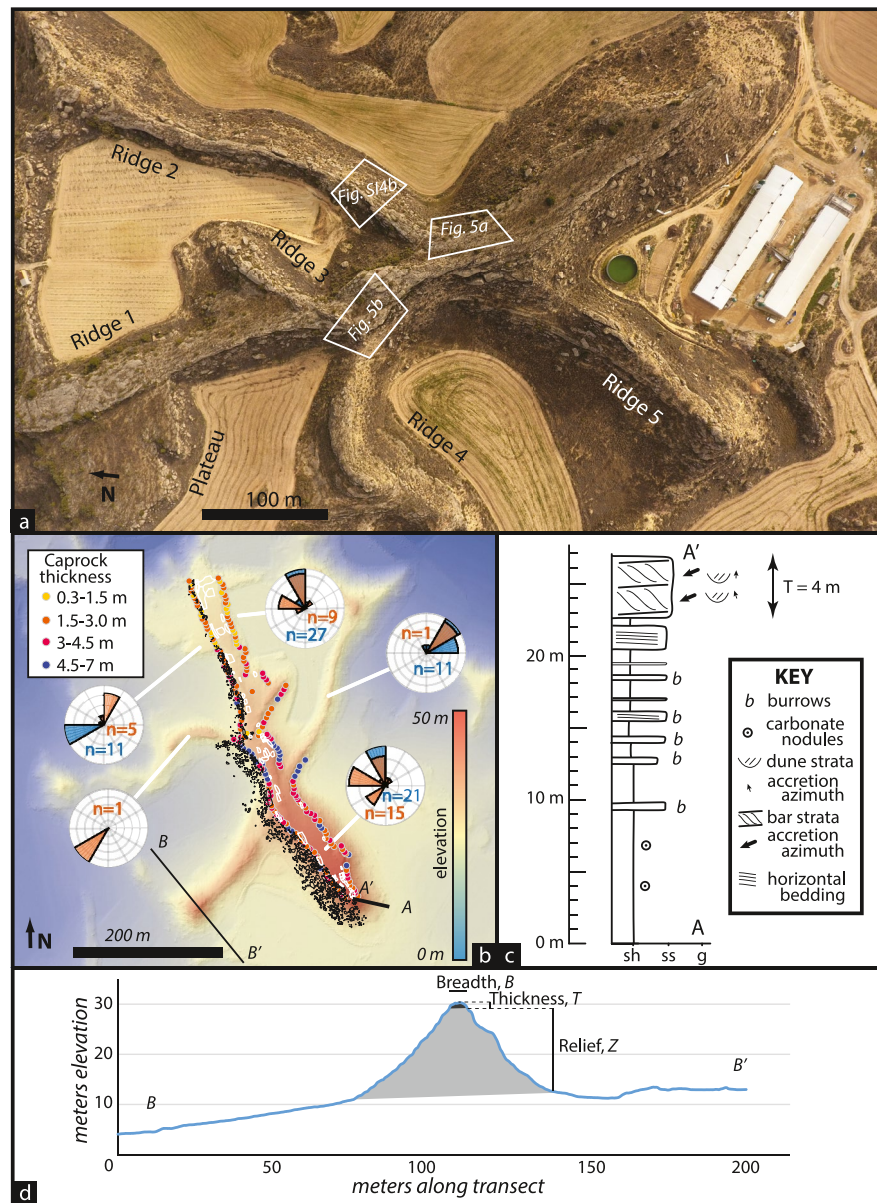


Figure 4. Site 4. (a) UAV photo showing the layout of the site, ridge names, and views used in subsequent figures. North is rotated $\sim 80^\circ$ counterclockwise. (b) Stratigraphic measurements of Site 4, showing accretion directions of dune sets (blue on rose diagrams) and bar clinoforms (red on rose diagrams). Black outlines are talus blocks (traced only on the west side of the ridge) and white outlines are cracks in the caprock. Locations of transects (A–A' and B–B') in (c and d) are shown, and black numbers indicate ridge numbers. (c) Representative stratigraphic section, the thickest of all the stratigraphic sections we measured. Location shown in white on (b). (d) Elevation transect across Ridge 5. The caprock and ridge flanks are identified by slope breaks in the transect; caprock is a cliff-forming unit and the base of the flanks are where the transect significantly flattens. Note that relief excludes caprock thickness following Hayden and Lamb (2020). Location is shown in black in (b).

Ridge flanks at Site 4 are covered in talus blocks made of the caprock sandstone. The dimensions of talus blocks are typically smaller than the width and thickness of the caprock (Figures 4b and 5a), and talus cover on the flanks ranged from 0%–70% by area (see west flank of Ridge 1 in Figure 4b). Talus blocks are totally absent beyond the base of the ridge flanks, but farming in those areas makes it unclear whether this is due to human modification or weathering. We noted extensive vertical cracks in Ridge 2, which suggests that talus blocks form by splitting off from the main caprock (Figures 5a and SI3b in Supporting Information S1).

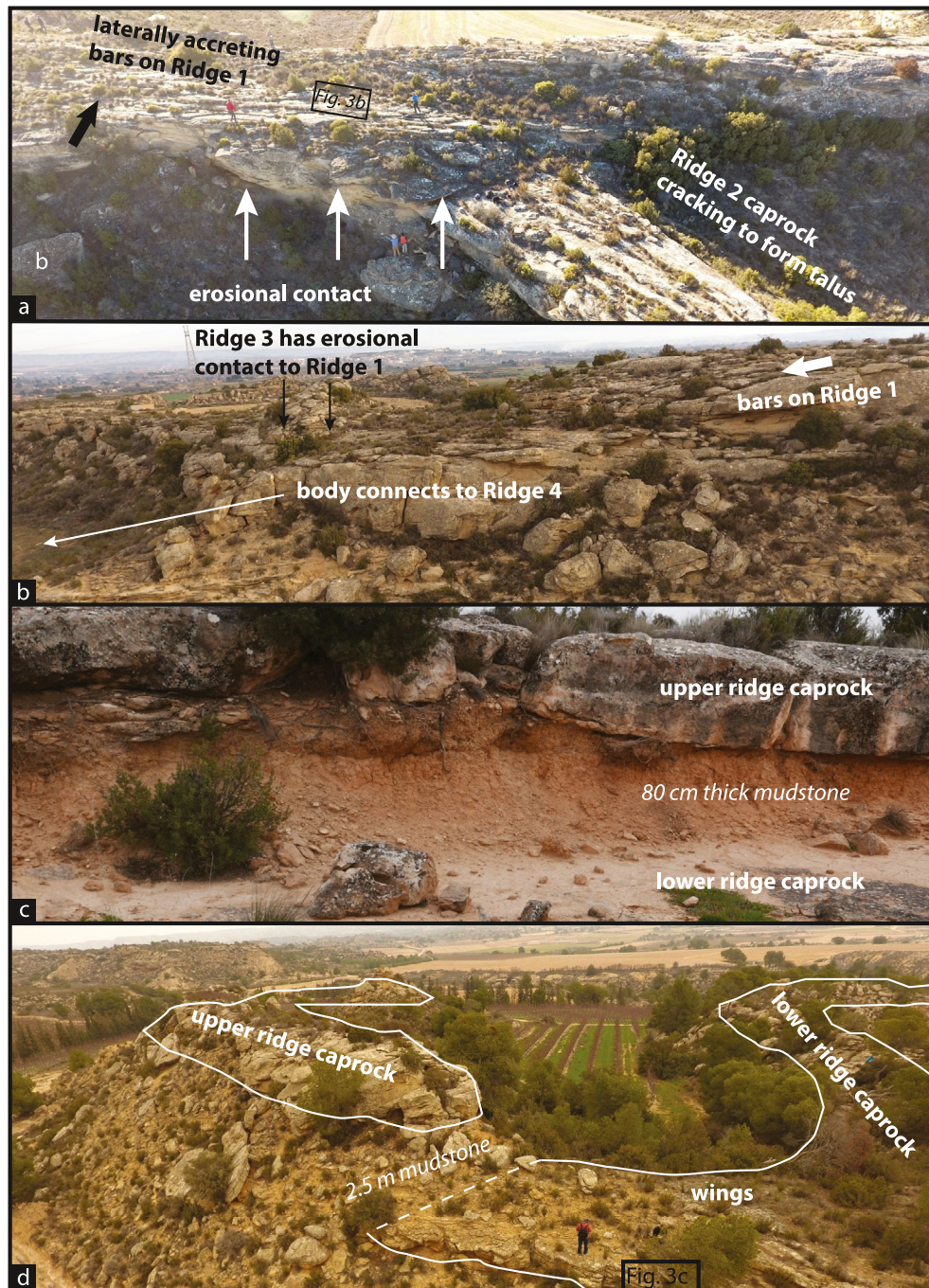


Figure 5. Different types of ridge intersection observed. (a) Oblique UAV photo of the intersection of Ridges 1 and 2 at Site 4 (location shown in Figure 4a), with people for scale. Though the ridges are at comparable stratigraphic levels, the channel body forming Ridge 1 erodes into that forming Ridge 2 (white arrows). Bars on Ridge 1 accrete (accretion direction given by black arrow) perpendicularly to the paleoflow direction interpreted from rib-and-furrow structures (Figure 3b; location shown in black box). This image also shows the caprock cracking to form talus, such as the large block that people are standing on between the white arrows, which appears to have come from Ridge 2. White letter “b” corresponds to Figure S14 in Supporting Information S1. (b) Another view of Ridge 1 at Site 4 with other channel bodies amalgamated with it. Ridge 3 is higher stratigraphically and shows an erosional contact with Ridge 1. Ridge 4 has no caprock at its intersection with Ridge 1, but there is a channel body amalgamated into the caprock of Ridge 1 that we interpret as previously connected to Ridge 4 on the basis of similar size and stratigraphic position. (c) An example of mudstone separating ridge caprocks from Site 5 (location shown in Figure 7c). (d) Larger separation of caprocks by mudstone from Site 7. This site appears to have branching ridges in planview, but in the field the caprocks of the ridges are separated by 2.5 m of mudstone and therefore are stratigraphically distinct. The upper ridge helps preserve the wings of the lower ridge, which pinch out laterally under the upper ridge. The location of the climbing dunes (Figure 3c) is shown.

The other field sites (Supporting Information) are largely similar to Site 4. All ridges comprise a cliff-forming caprock of fine to medium sandstone atop ridge flanks of dominantly mudstone with some thin sandstone sheets. Caprocks have abundant dune cross-strata 0.03–0.70 m thick. In one case we observed climbing dunes (Figure 3c); these have accretion directions away from the channel axis and occur in the thinnest part of the caprock, near the edge. Caprocks also have abundant truncated bar cross-strata 0.30–3.0 m thick (e.g., Figures 6a and 6b), which have accretion directions ranging from parallel to perpendicular to the paleo-flow directions as indicated by the dune cross-strata dip directions or paleo-channel banks as indicated by scour surfaces. Site 6 shows a point bar complex that is higher in stratigraphic position on the outside of the bend (Figure 7a), suggesting the river aggraded as it migrated laterally during channel-bend growth. Site 2 has bar-accretion directions both toward and away from planview convexity of the ridge (Figure 7b), indicating that modern ridge geometry can be independent of paleochannel geometry because channels are expected to migrate in the direction of their convexity whereas the ridge shows accretion opposite the expected direction. We inferred paleo-channel bed aggradation, in addition to bar lateral accretion, based on observations of truncated bar strata stacked vertically at some locations (e.g., Figures 6a and 6b).

In most cases, ridge junctions represent caprocks crossing at distinct stratigraphic levels, rather than tributary or distributary bifurcations. Stacked caprocks are typically separated by mudstone at their junctions (e.g., Figures 5c and 5d), suggesting periods of channel abandonment. Other junctions show sandstone amalgamation, with the channel body forming the upper caprock cut into the channel body of the lower caprock (Figure 5). Site 5 shows additional evidence for amalgamation; two sandstone bodies separated by mudstone (Figure 7c) are amalgamated together for 100 m along the ridge length before separating again by mudstone. This is an example of how smaller channel belts can amalgamate to form wider or thicker channel-belt sandstone bodies. For this ridge, the amalgamated section is slightly wider, but not significantly thicker, which can be due to scouring preceding later deposition. Site 8 shows ridges stacked atop a cliff-forming sandstone sheet, which is formed from laterally accreting bars (Figure S18 in Supporting Information S1).

In addition to the ridges, there are non-ridge-forming (non-eroded) sandstone bodies in cliff outcrop (e.g., Figure 6a) and in road or railroad outcrops that make useful comparisons. These sandstone bodies range from 1.5 to 120 m wide and 1.9 to 18.8 m thick, with width–thickness ratios of 2–28. All have dune cross-stratification and truncated bar clinofolds. The bar clinofolds generally have aggradation directions perpendicular to the main axis of the body, indicating lateral bar accretion. Most channel bodies significantly thin toward their edges (e.g., Figure 6a).

Measurements from ridges and unexhumed channel bodies are summarized in Figure 8, including remote-sensing measurements of caprock dimensions, similar to those that can be made for ridges on Mars (Figures 8a–8c), and field measurements of grain size (Figure 8d), thickness of cross-strata (Figure 8e), and breadth of unexhumed channel bodies (Figure 8f) that can only be made with in-situ observation. Caprock thicknesses (Figure 8a) measured in the DEMs range from 1.9 to 6.1 m for our field sites, and have a 5–95 percentile range of 0.6–4.3 m across the whole fan, and uneroded channel-body thicknesses measured in the field were similar with a 5–95 percentile range of 1.3–7.8. Caprock widths measured in the DEMs range from 8.5 to 44 m for our field sites, and have a 5–95 percentile range of 10–45 m for ridges across the whole fan, whereas non-ridge channel-body breadths were wider with a 5–95 percentile range of 8.1–78 m (Figures 8b and 8f). Caprock relief measured in the DEMs range from 3.5 to 26 m for ridges at field sites and have a 5–95 percentile range of 0–10 m for all ridges, whereas non-ridge channel-body relief values (measured in the field as the vertical distance between channel-body bottom and cliff bottom) have a 5–95 percentile range of 7.8–46 m (Figure 8c). Grain sizes for caprocks (Figure 8d) at our field sites range from fine to coarse sandstone (0.2–0.5 mm), whereas grain sizes at uneroded channel bodies were generally similar, but much coarser (up to 20 mm) at locations closer to the fan apex (further south).

4.2. Paleo-Hydraulics

On Earth, the sediment discharge of ancient rivers can be constrained from measurements of sedimentary structures, such as dune and bar strata, though such observations are rare for Mars (e.g., Stack et al., 2019; Williams et al., 2013). Where well preserved, exposed, and visible from orbit, fluvial ridges preserve information about fluvial deposits that can be used to constrain paleochannel bankfull geometry (e.g., Burr et al., 2010; Kite, Howard, Lucas, & Lewis, 2015). Therefore, we calculated paleo-hydraulics using remote-sensing measurements with

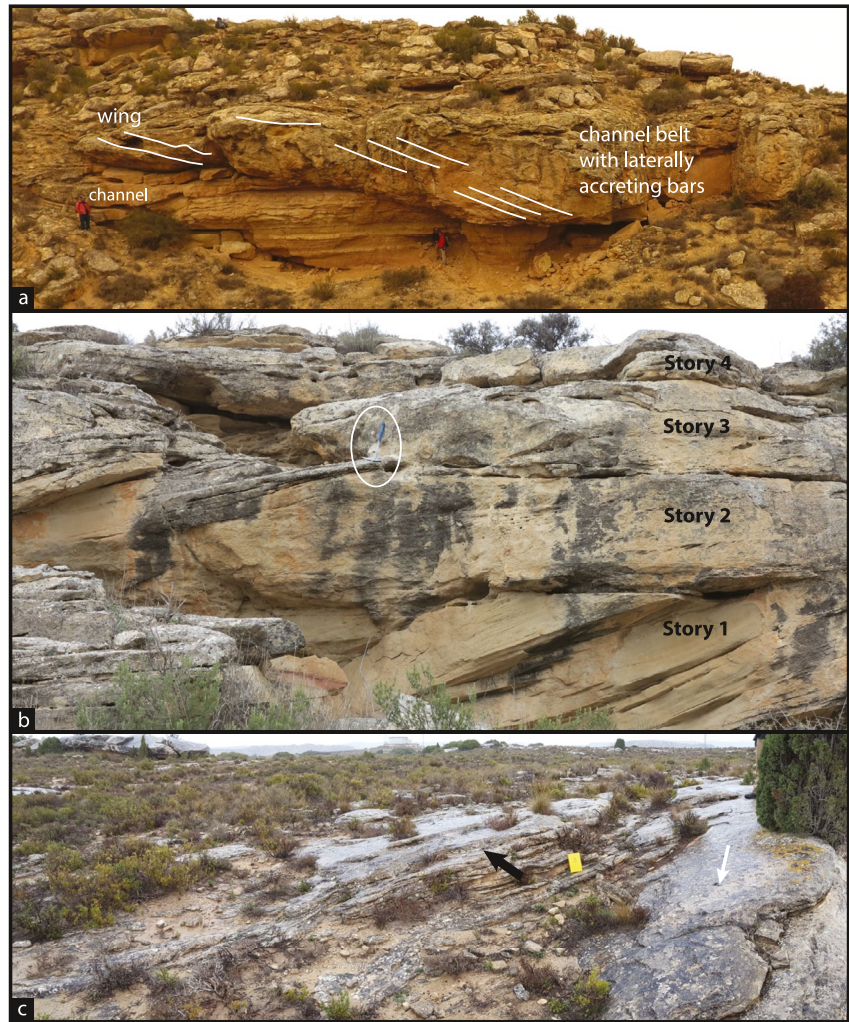


Figure 6. Field observations of bar cross-strata. (a) UAV photo of a channel belt at Site 8 that incises into pre-existing floodplain deposits, including small channel conduits that could be crevasse-splays. The channel belt contains multiple levels of internal stratification that appear to be bars, indicating vertical aggradation. (b) Stacked bar structures that truncated earlier structures as the channel belt built up at Site 6 (hammer, circled, for scale). Location is shown in Figure 7a. (c) Bar strata (41.068°N, 0.161°W) accrete (black arrow) perpendicular to paleoflow direction (white arrow). Yellow notebook (12 cm × 19 cm) for scale.

methods typically used for Mars, and, separately, using sedimentology measurements with methods common for Earth. Following prior work in the Guadalupe-Matarranya fan (Mohrig et al., 2000), we assumed flows were consistent across the basin and combined values at all measurement locations into a single reconstruction.

The mean height of 242 dune cross strata was 0.14 m (Figure 8e), which by Equation 3 yielded a mean paleochannel depth of 1.4 m. The mean height of 13 truncated bar clinofolds is 0.6 m (Figure 8e), which by Equation 2 yielded a minimum mean paleochannel depth of 0.6 m. The median thickness of 131 channel belts measured in cliff outcrops was 3.6 m and the median thickness of ridge caprocks was 1.7 m (Figure 8g), which by Equation 4 yields paleochannel depths of 2.4 and 1.1 m, respectively. There is agreement in depth reconstructions between sedimentology and caprock thickness reconstructions (Figure 8h); we used the mean paleochannel depth averaged across the four different methods of 1.4 m. Prior work reports flow depths interpreted from bar thickness that range from 1 to 3.3 m, with little variation with stratigraphic level and across the fan system (Mohrig et al., 2000), and these also have a mean value of 1.4 m.



Figure 7. UAV images illustrating amalgamation. White arrows indicate paleoflow directions and black arrows indicate bar accretion directions. (a) Site 6 exhibits exhumed point bars that accrete perpendicularly to the flow direction, toward the outside of the bend. The channel belt built vertically as it aggraded laterally so the stratigraphic position increases to the outside of each bend. Location of Figure 6b shown. (b) High-sinuosity ridge at Site 2 exhibits bars accreting in the direction of ridge planview concavity, indicating that the ridge is a channel belt rather than a channel cast. (c) Two ridges at Site 5 that join and then separate after 100 m. The location of Figure 5c is shown.

4.3. Intermittency Factor

We used our measurements of ridge-bearing area (3000 km²) and stratigraphic thickness (0.7 km), estimated sand fraction of $f = 0.25$, and porosity of $\lambda = 0.31$ (Buj & Gisbert, 2010) to calculate a sand and gravel volume of 362 km³. The calculated stratigraphic thickness is consistent with a previously estimated lower bound of 0.4 km (Barbera et al., 2001; Cuevas Martínez et al., 2007, 2010). Using the paleochannel depth of 1.4 m and the median grainsize of $D_{50} = 0.25$ mm in Equations 5–11 results in a bankfull sediment discharge of $Q_{s,bf} = 0.48$ m³/s. Combining this sediment discharge estimate with the depositional timespan ($\Sigma t = 6$ Myr) in Equation 1, we calculated an intermittency factor of $I_f = 0.004$ (uncertainty: 0.0004–0.04) for the Guadalupe-Matarranya fan.

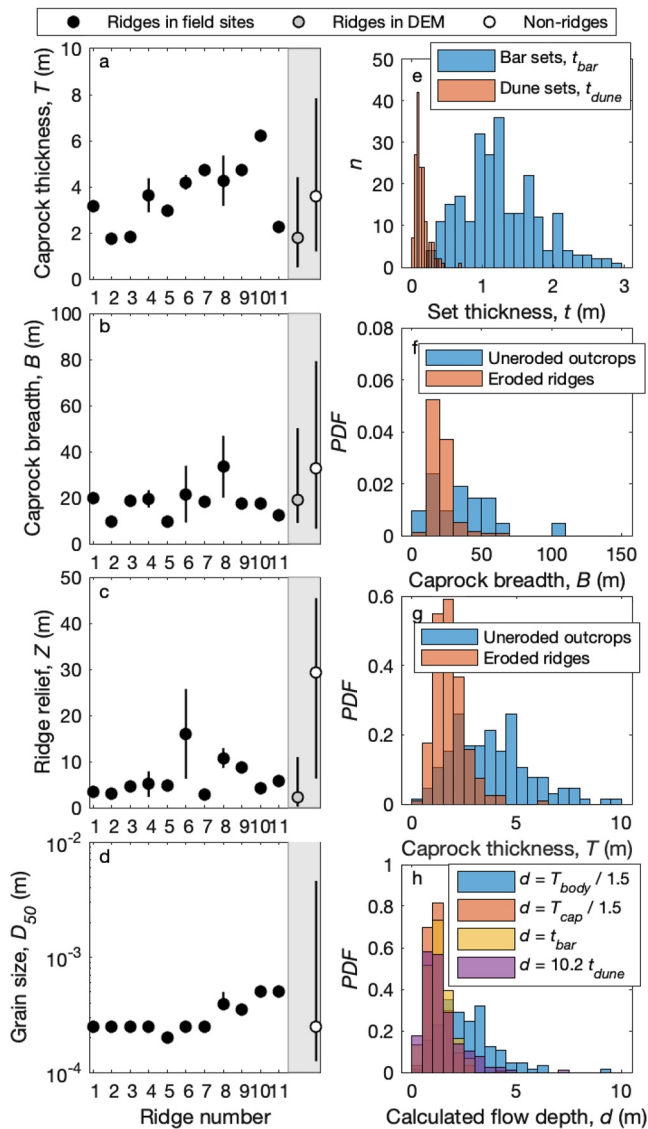


Figure 8. Data from the field sites studied in detail, ridges studied in the lidar DEM, and non-ridge-forming channel bodies in cliff outcrop. Measurements of caprock thickness (a), caprock breadth (b), relief above surrounding plains [(c) for non-ridges in outcrop, relief is measured from the bottom of the channel body to the bottom of the cliff that exposes it], and median grain size (d) for each field area and of non-ridge-forming channel bodies. Also, shown are observations of thickness of truncated dune sets and truncated bar sets (e), breadth (f), and thickness (g) of uneroded channel bodies in outcrop measured in the field and of eroded ridges measured in the lidar DEM, and calculations of flow depth (h) from the different input parameters in (e) and (g), using methods described in Section 3.2.

In comparison, Figure 9 shows calculated sediment-transport intermittency factors between 0.0064 to 0.73 for 207 modern terrestrial rivers and modern and ancient fans and deltas (Hayden, Lamb, & McElroy, 2021). Hayden, Lamb, and McElroy (2021) found that intermittency factor is independent of bed-material grain size (Figure 9a). The Guadalupe-Matarranya fan plots to the low end of the values they measured, indicating very intermittent sediment transport. It might be expected that the intermittency factor would change with averaging timescale due to climate and tectonic variability, but they found that intermittency factors span similar values across a wide variety of timescales. Similarly, we calculated an intermittency factor for the Guadalupe-Matarranya fan that is comparable to values estimated for both modern rivers and other ancient depositional systems (Figure 9b).

5. Discussion

5.1. Interpretation of the Ridges of the Guadalupe-Matarranya Fan

Studies of terrestrial fluvial ridge show they can be divided into two broad types: channel casts known as *inverted channels* (Burr et al., 2009; Pain & Ollier, 1995), and channel-belt deposits known as *exhumed channel belts* (DiBiase et al., 2013; Hayden et al., 2019). Inverted channels form when a channel is filled with an erosion-resistant material such as lava or coarse sediment and the neighboring material is eroded away, leaving a ridge with a width that may approximate the original channel form; such forms allow bankfull geometries to be measured from orbit (e.g., Burr et al., 2010). Alternatively, ridges that formed as exhumed channel belts reflect the geometry of the channel belt, the region of amalgamated, relatively coarse-grained river deposits that form from river lateral migration and aggradation (DiBiase et al., 2013; Hayden et al., 2019).

We interpret the ridges in the Guadalupe-Matarranya fan to be exhumed and eroded channel belts, rather than inverted channels, similar to previous work in the area (Cuevas Martínez et al., 2007, 2010; González-Bonarino et al., 2010; Friend et al., 1979; Mohrig et al., 2000; Williams, 1975). Ridge caprocks exhibit amalgamated strata from dunes and bars (Figures 3 and 6), indicating channel aggradation and channel lateral migration created a channel belt. Sandstone “wings” (Mohrig et al., 2000), one of which has climbing dunes that indicate rapid aggradation with flow direction away from the channel axis (Figure 3b), are interpreted as overbank levee deposits that downlap onto the floodplain and are characteristic of channel-belt deposits (Allen et al., 1983; Friend et al., 1979). The caprocks are typically thicker than the reconstructed paleochannel depth (Figure 8) and dune strata do not change up section (Cuevas Martínez et al., 2007, 2010), suggesting channel-bed aggradation and/or channel reoccupation by successive generations of fluvial activity. In contrast, channel fills (which are needed to make topographically inverted channels) would be expected to be fine-grained and have decreasing flow depths up section, as an abandoned channel pathway fills with overbank material (Nichols & Fisher, 2007). Finally, ridge junctions reflect crossings of channel belts formed at distinct stratigraphic intervals,

in some cases separated by mudstone (Figures 5c and 5d) and in other cases with no separation between channel belts (Figures 5a and 5b and 7c), indicating fluvial stratigraphy built over long durations rather than a preserved channel network preserved in inverted relief. These observations and interpretations are similar to those made for exhumed channel belts in the Morrison Formation (Hayden & Lamb, 2020) and Cedar Mountain Formation (Cardenas et al., 2020; Hayden et al., 2019; Williams et al., 2009) in Utah, USA.

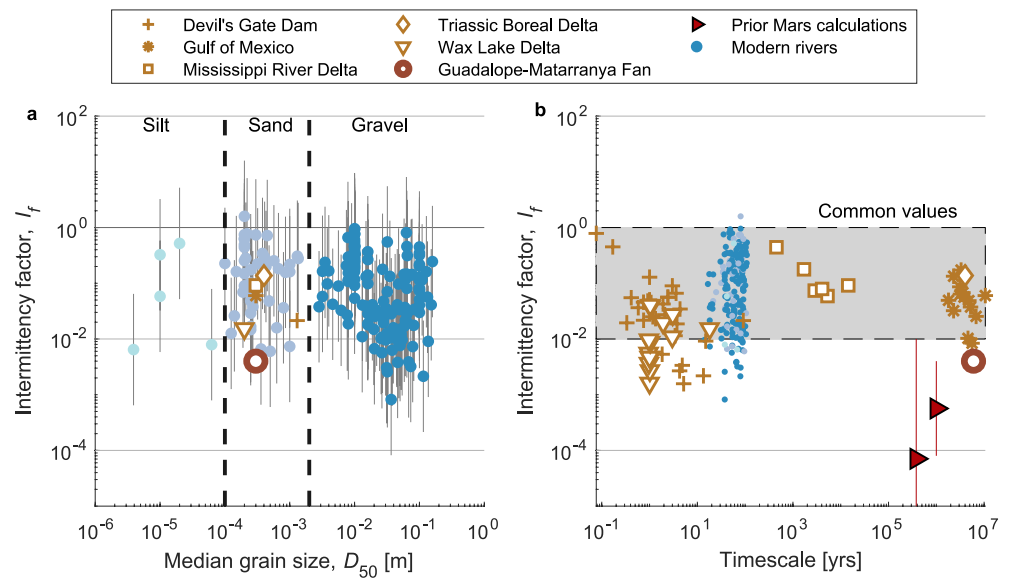


Figure 9. Values for intermittency factor for modern rivers and ancient sedimentary deposits from Hayden, Lamb, and McElroy et al. (2021). Uncertainty bars represent a combination of uncertainty in channel geometry and in calculating sediment discharge, and bars for prior calculations for Mars represent reported range of acceptable values. Y-axis is the intermittency factor for all panels, X-axis is grainsize (a) or timescale (b). Blue dots and all brown symbols except the circle are values from Hayden, Lamb, McElroy et al. (2021), and red triangles (b only) are values calculated for martian deposits (Buhler et al., 2014; Lapôtre & Ielpi, 2020).

Multiple lines of evidence indicate that the ridges eroded by scarp retreat, similar to exhumed channel belts elsewhere on Earth (e.g., Hayden & Lamb, 2020). Quantitatively, ridge breadths (10–50 m) are tens of meters smaller than the breadths of uneroded channel belts (up to 80 m), whereas thickness is only a few meters smaller for ridge caprocks as compared to uneroded channel belts (Figure 8). Talus blocks are abundant on ridge flanks and cross-strata are visible on caprock edges, directly implicating erosion. Furthermore, bar accretion sets often extend to the caprock edges, indicating that the channel at the leading edge of the bar is not preserved within the caprock strata (e.g., Figure 5a).

Distinguishing ridges as exhumed and eroded channel belts rather than inverted channels is important because it helps select tools to reconstruct paleo-hydraulics, and because it suggests different timespans of fluvial deposition. Whereas ridge width, wavelength, and radius of curvature might be good proxies for their respective paleochannel counterparts under the inverted channel model (e.g., Burr et al., 2010; Kite, Howard, Lucas, & Lewis, 2015), those measures can be inaccurate when applied to exhumed channel belts (Hayden et al., 2019; Hayden & Lamb, 2020; Hayden, Lamb, & Carney, 2021). Instead, caprock thickness or lateral-accretion-set radius of curvature can be used to reconstruct paleochannel depth or width, respectively, when exhumed channel belts are interpreted (Hayden et al., 2019; Hayden & Lamb, 2020). The timespan of fluvial activity suggested by a fluvial ridge also depends on the interpretation of its origin—exhumed channel belts must have been deposited over timespans that allowed lateral migration and vertical aggradation (e.g., Lapôtre & Ielpi, 2020), whereas inverted channels only require fluvial activity sufficient to carve a channel. The precise timespan still must be calculated in either case, but exhumed channel belts suggest longer durations of fluvial activity.

Though we interpret ridges in the Ebro Basin as channel belts, ridge dimensions are fairly similar to the reconstructed paleochannel dimensions. Ridge caprocks are 0.1–2 times wider than the median paleochannel, and have thickness 0.3–4 times the median paleochannel depth. Channel-belt thickness is expected to be within a factor of four of paleochannel depth (Hayden et al., 2019), due to the tendency for rivers to avulse and abandon a channel belt after they aggrade by an amount that scales to first order as the channel depth (Ganti et al., 2014; Mohrig et al., 2000; Slingerland & Smith, 2004). Channel belts can be thicker if there is amalgamation due to channel-belt reoccupation, but reoccupation might also begin with scour that removes the prior deposit and results in similar thickness before and after reoccupation (e.g., Figure 7c).

The similarity in measured ridge breadth to calculated paleochannel width is more surprising. We observed two factors that are potentially important in setting this observation. First, channel lateral migration can create a channel belt that is wider than the channel width. Second, scarp retreat during ridge exhumation can narrow the ridge caprock with respect to the original channel-belt. Therefore, it seems that the effects of channel lateral migration and ridge lateral erosion by scarp retreat offset by comparable amounts on average to make ridge widths statistically similar to paleochannel widths. This similarity also has been observed for exhumed channel belts in the Cedar Mountain Formation (Hayden et al., 2019) and Morrison Formation (Hayden & Lamb, 2020). Uneroded channel belts at all three sites are relatively narrow ($B/T < 30$)—close to the dimensions of ribbon sandstones (Friend et al., 1979)—whereas channel belt widths can be substantially larger at other sites ($B/T > 50$; e.g., Robinson & McCabe, 1997). The reason we do not see very wide ridges might be that wide channel belts would tend to amalgamate laterally with other channel belts at similar stratigraphic levels, forming a sheet-like sandstone body. In the Ebro basin, we observed that wide sandstone bodies tend to form mesas and plateaus rather than ridges. For example, Site 8 has small ridges perched atop a mesa exhibiting lateral accretion (Figure S18 in Supporting Information S1).

5.2. Intermittency Factor

The intermittency factor we found for the Guadalupe-Matarranya fan of $I_f = 0.004$ (uncertainty: 0.0004–0.04) is among the lowest 5% of values that were calculated for terrestrial systems by Hayden, Lamb, & McElroy (2021) (Figure 9). A low intermittency factor for the Guadalupe-Matarranya fan is supported by field observations. Cuevas Martínez et al. (2007, 2010) observed pedogenically altered mudstone laminae between some downstream-accreting bars and putative ant nests within the bars, both of which they interpreted to represent intermittent fluvial activity. González-Bonarino et al. (2010) also found bioturbation and small-scale sedimentary structures and interpreted that low or no flows existed between the main bar-forming flood events. Milankovitch-cycle-paced cyclicity is also evident in the lacustrine deposits of the Los Monegros Formation at the toe of the Guadalupe-Matarranya fan system (Pérez-Rivarés et al., 2004; Valero et al., 2014).

Hayden, Lamb, and McElroy (2021) found that the intermittency factor correlates with the ratio of catchment-averaged denudation to precipitation, suggesting that rivers with a low relative sediment to water supply transport sediment less often (or under conditions less like continuous bankfull flow). Though Hayden, Lamb, and McElroy (2021) were unable to disentangle the effects of catchment-averaged denudation versus precipitation, it is well established that both environmental parameters are important controls on channel dynamics (e.g., Mackin, 1948; Parker et al., 2007). The value of $I_f = 0.004$ is similar to the values of rivers in the modern Appalachian Mountains, which are humid and eroding relatively slowly. Though the Guadalupe-Matarranya fan comprises sediment from the Catalan Coastal and Iberian Ranges, which were active during the early Miocene when the fan was forming (Anadon et al., 1989) and therefore likely had higher denudation rates than the modern Appalachians, a number of small piggyback basins in the source area (e.g., González & Guimerá, 1993) trapped an important part of the coarse fraction before it entered the Ebro Basin. The sediment supply reaching the Guadalupe-Matarranya fan was therefore likely low. The Ebro Basin is thought to have been semi-arid during the Miocene (e.g., Cabrera et al., 1985), which also could have resulted in slow weathering and sediment production.

The value of intermittency factor for the Guadalupe-Matarranya fan is indistinguishable from intermittency factors calculated for modern rivers by Hayden, Lamb, and McElroy (2021), despite averaging over a much longer timescale (6 Myr) and a much larger spatial scale (an entire mega-fan vs. a single river reach). This might be unexpected due to prior observations that deposition rates are inversely correlated with averaging timescale (Sadler, 1981). However, the Sadler effect may not bias data when entire deposit volumes are evaluated (e.g., Hayden, Lamb, & McElroy, 2021; Sadler & Jerolmack, 2015). An alternative explanation, which could be simultaneously true, is that, because there were not major tectonic or climatic changes, the calculated intermittency factor for the Guadalupe-Matarranya fan might exclude additional intermittency sources that could be present elsewhere.

5.3. Application of Depositional Duration Calculations to Mars

The methods we developed and evaluated in the Ebro basin can be applied to Mars. DEMs exist from the Mars Orbital Laser Altimeter (463 m/px) for all of Mars, and more detailed models can be made using stereopairs of

Table 1
Comparison of Depth Reconstructions From Remote Sensing Versus Sedimentologic Observations

Method	Raw measurement [mean (standard deviation, number of measurements)]	Calculated bankfull depth, H_{bf}
Dune set thickness (Equation 3)	$t_{dune} = 0.14$ m (0.1, $n = 242$)	1.4 m
Bar clinoform thickness (Equation 2)	$t_{bar} = 0.6$ m (0.5, $n = 13$)	0.6 m
Ridge caprock thickness (Equation 4)	$T_{caprock} = 1.7$ m (0.8, $n = 6222$)	1.1 m
Uneroded channel belt thickness (Equation 4)	$T_{belt} = 3.6$ m (2.4, $n = 131$)	2.4 m
Average across methods		1.4 m

CTX or HiRISE imagery that approach the resolution of the lidar DEMs used for Ebro in this study. On Mars, stratigraphic thickness has been interpreted from elevation by assuming approximately flat-lying deposits (cf., Kite et al., 2013). The area covered by sinuous ridges correlates well with the mapped outcrop of the Guadalupe-Matarranya fan (Figure 2); similarly, the area of fluvial outcrop can be measured from orbit on Mars as the ridge-bearing region. Porosity is set by packing geometry and should be close to 0.3–0.35, assuming well-sorted material. Coarse-sediment fraction (volume-fraction of sand or gravel) range between 20% or 80% in terrestrial fluvial deposits (Heller et al., 2015). Ridges form where channel belts are surrounded by mudstone and the mudstone is preferentially eroded (DiBiase et al., 2013). With larger coarse-sediment fraction, the channel belts would amalgamate and form mesas when exhumed. Therefore, the presence of ridges rather than mesas implies that the coarse-sediment fraction is low but nonzero. Thus, with assumed values of porosity and coarse-sediment fraction that likely vary little, Equation 12 can be used to calculate sediment volume using orbital measurements.

Paleochannel depth on Mars can be estimated from ridge caprock thickness using Equation 4, which yielded the same paleochannel depth as reconstructions from cross-strata thickness (Figure 8h and Table 1). Equation 4 is expected to hold on Mars because it is based on avulsion thresholds, where a river aggrades the thickness of approximately one channel depth before becoming unstable and switching course (Ganti et al., 2014; Mohrig et al., 2000; Slingerland & Smith, 2004). Grainsize is the other value to calculate sediment discharge from Section 3.3. No in situ measurements exist for grainsize of martian fluvial ridges, but values between 0.2 and 100 mm are typically used based on investigation at other deposits on Mars (e.g., Kleinbans, 2005; Stack et al., 2019; Williams et al., 2013) and justified based on similarity to typical rivers on Earth (e.g., Hayden et al., 2019).

Combining the orbit-based estimates of outcrop area, stratigraphic thickness, and paleochannel depth with estimates of porosity, coarse-sediment fraction, grainsize, and intermittency factor enables calculation of duration of a fluvial system with Equation 1. Of the estimated parameters, grainsize and intermittency factor would benefit from additional precision in estimates for ancient fluvial systems on Mars. Crater-dating methods could also be applied to estimate depositional durations, such as the embedded-crater counts performed by Kite et al. (2013).

5.4. Implications for Mars

The Guadalupe-Matarranya fan has many similarities to megafans on Mars. As an example, we focused on a large branching ridge network from the Aeolis Dorsa region of Mars (Figure 1b), which we refer to as network X. Network X has been interpreted as a distributary network mapped as part of a larger system covering 2700 km² (Lefort et al., 2015), and it therefore would be classified as a megafan. Previous work (Hayden et al., 2019) identified ridge stacking patterns (Figure 1c) that indicate channel belts exhumed from different stratigraphic levels, similar to the Guadalupe-Matarranya fan. Kite et al. (2013) measured at least 300 m of fluvial stratigraphy in a broader region that includes network X. Combining $A = 2700$ km² and $F = 0.3$ km in Equation 12 with the values we used for the Guadalupe-Matarranya fan for $\lambda = 0.35$ and $f = 0.25$, we found $V = 134$ km³. This volume is half that of the Guadalupe-Matarranya fan. A comparable depositional duration exceeding 1 Myr for network X aligns with the findings of Kite et al. (2013), who, based on embedded-crater counting, found a duration of millions of years of river activity for a broad portion of Aeolis Dorsa that contains this location. However, the caprock thicknesses measured on one ridge have a median value of 13 m (Hayden & Lamb, 2020), suggesting rivers 9 m deep—six times deeper than the depth we reconstructed for the Guadalupe-Matarranya fan, which implies significantly more water during flow events, and possibly a shorter depositional duration. A final similarity

of our analog site is that its semi-arid climate (Cabrera et al., 1985) is similar to that interpreted for early Mars (e.g., Stucky de Quay et al., 2020).

Other megafans on Mars (e.g., Figure 1a) appear similar to the Guadalupe-Matarranya fan. For instance, there are several known megafans that also cover large areas, such as Hypanis Valles Delta ($A = 1000 \text{ km}^2$; Adler et al., 2018; Fawdon et al., 2018) and the delta in Figure 1a (DiBiase et al., 2013; $A = 2100 \text{ km}^2$). These and other potential megafans exhibit fluvial ridges (e.g., Cardenas et al., 2018; DiBiase et al., 2013; Hughes et al., 2019; Lefort et al., 2015), so the techniques used here can be applied to Mars. Importantly, the Perseverance rover will be able to provide *in situ* analysis of bar and dune structures in Jezero Crater, enabling reconstruction of paleo-channel parameters following Equations 2 and 3 that can be compared to remote-sensing reconstructions (e.g., Goudge et al., 2018; Lapôtre & Ielpi, 2020).

One major difference between the Guadalupe-Matarranya fan and megafans on Mars is the role played by tectonics in forming accommodation space for the sediment. Strata on Earth typically are deposited into a basin formed by subsidence, whereas Mars appears to generally lack the tectonics that would create basins, though some evidence of tectonics exists (e.g., Davis et al., 2021). On Mars, impact basins may provide accommodation space, but they do so instantaneously rather than through dynamic flexure and subsidence (e.g., Grotzinger & Milliken, 2012). The effect of tectonic quiescence on stratigraphic thickness is unclear. The few existing measurements of thickness of fluvial stratigraphy for Mars (e.g., $>0.3 \text{ km}$ for inter-crater plains in Aeolis Dorsa [Kite et al., 2013] and $>1 \text{ km}$ for the delta inside Terby Crater; Ansan et al., 2011) are similar to common stratigraphic thicknesses on Earth. However, tectonic quiescence complicates measurement of stratigraphic thickness because, without crustal deformation, layers remain flat-lying, rendering it impossible to measure thickness without focused erosion exposing part of the deposit. For sedimentary deposits in impact basins, the initial geometry of craters can be used to estimate possible deposit dimensions (e.g., Kleinhans et al., 2010), but many deposits, including those of Aeolis Dorsa, are outside a recognizable impact basin (Dickson et al., 2021). Therefore, it is likely that many estimates of stratigraphic thickness of fluvial stratigraphy on Mars represent minimum bounds on the true values, making the estimated depositional timescales minimum bounds as well.

The intermittency factor has been assumed to be between $I_f = 0.001$ and 1 in many studies on Mars (e.g., Kleinhans et al., 2010; Morgan et al., 2014; Orofino et al., 2018). The value of intermittency factor we calculated for the Guadalupe-Matarranya fan is on the low end of this range, supporting the idea of long-lived fluvial systems on Mars, including some that exceed millions of years (Hayden, Lamb, McElroy, 2021). There are only two cases where I_f was estimated directly on Mars (Buhler et al., 2014; Lapôtre & Ielpi, 2020); both cases found even smaller values ($I_f \cong 0.0001$), which would make depositional timespans even longer, but there is significant uncertainty inherent in the estimates due to the loosely constrained depositional timespan. Timescales exceeding millions of years are inconsistent with short, intermittent clement climates that last on the scale of centuries (e.g., Halevy & Head, 2014). However, the likely durations are shorter than the 10^8 year timescale of the entire Noachian.

6. Conclusions

The Guadalupe-Matarranya fan in the Ebro Basin of Spain contains many exhumed channel belts, expressed as fluvial ridges, and is an excellent analog for similar features observed across Mars that might also represent exhumed megafans. Thickness of the channel bodies, as well as cross-stratification from bars and dunes, indicates that the deposit was created by sand-bedded rivers $\sim 1.4 \text{ m}$ deep, which we used to estimate a representative bank-full sediment discharge of $0.48 \text{ m}^3/\text{s}$. Using the total sediment volume of the fan (362 km^3) and the depositional timespan (6 Myr), we estimated the intermittency factor was 0.004 (probable range: 0.0004–0.04).

Remote-sensing measurements yielded similar results; ridges cover most of the area mapped as Guadalupe-Matarranya fan and therefore are indicators of fluvial deposits visible from orbit, and paleochannel depth reconstructions from DEM measurements of ridge caprock thickness are indistinguishable from the reconstructions based on field observation of sedimentology. The analysis presented here therefore can be applied to fluvial deposits on Mars using only orbital datasets.

The intermittency factor we calculated for the Guadalupe-Matarranya fan is among the lowest values estimated on Earth, and is lower than most values previously assumed for fluvial systems on Mars. Applying the intermittency

factor of 0.004 (uncertainty: 0.0004–0.04) to prior calculations of durations of fluvial systems on Mars suggests timespans of fluvial activity for individual systems lasting millions of years or longer. These results support the hypothesis that rivers during the late Noachian/early Hesperian could have persisted over substantial geologic time.

Data Availability Statement

The Supporting Information document includes additional description of the field sites. All data are included here: <http://dx.doi.org/10.22002/D1.2174>.

Acknowledgments

This work was supported by NASA (grant NNX16AQ81G1960 to MPL and graduate fellowship support 80NSSC17K0492 to ATH), Project SEROS and Grup de Recerca Consolidat 2017-SGR467 of the Generalitat de Catalunya to JLCM. The authors have no financial conflicts of interest. We are grateful to Mackenzie Day and an anonymous reviewer for excellent feedback that improved the manuscript.

References

- Adler, J. B., Bell, J. F., Fawdon, P., Davis, J., Warner, N. H., Sefton-Nash, E., & Harrison, T. N. (2018). Hypotheses for the origin of the Hypanis fan-shaped deposit at the edge of the Chryse Escarpment, Mars: Is it a Delta? *Icarus*. <https://doi.org/10.1016/j.icarus.2018.05.021>
- Allen, J. R. (1963). The classification of cross-stratified units. With notes on their origin. *Sedimentology*, 2(2), 93–114. <https://doi.org/10.1111/j.1365-3091.1963.tb01204.x>
- Allen, J. R. (1965). A review of the origin and characteristics of recent alluvial sediments. *Sedimentology*, 5(2), 89–191. <https://doi.org/10.1111/j.1365-3091.1965.tb01561.x>
- Allen, P., Cabrera, L., Colombo, F., & Matter, A. (1983). Variations in fluvial style on the Eocene–Oligocene alluvial fan of the Scala Dei Group, SE Ebro Basin, Spain. *Journal of the Geological Society*, 140(1), 133–146. <https://doi.org/10.1144/gsjgs.140.1.0133>
- Anadón, P., Cabrera, L., Colombo, F., Marzo, M., Colldeforns, B., Cuevas Martínez, J. L., et al. (1989). Alluvial fan evolution in the SE Ebro basin: Response to tectonics and lacustrine base level changes. *4th International Conference on fluvial sedimentology*. Generalitat de Catalunya, Departament de Política Territorial i Obres Públiques, Secretaria General, Servei Geològic de Catalunya.
- Ansan, V., Loizeau, D., Mangold, N., Le Mouélic, S., Carter, J., Poulet, F., et al. (2011). Stratigraphy, mineralogy, and origin of layered deposits inside Terby crater, Mars. *Icarus*, 211(1), 273–304. <https://doi.org/10.1016/j.icarus.2010.09.011>
- Baker, V. R., & Partridge, J. B. (1986). Small Martian valleys: Pristine and degraded morphology. *Journal of Geophysical Research: Solid Earth*, 91(B3), 3561–3572. <https://doi.org/10.1029/jb091ib03p03561>
- Barberà, X., Cabrera, L., Marzo, M., Parés, J. M., & Agustí, J. (2001). A complete terrestrial Oligocene magnetobiostratigraphy from the Ebro Basin, Spain. *Earth and Planetary Science Letters*, 187(1), 1–16. [https://doi.org/10.1016/S0012-821X\(01\)00270-9](https://doi.org/10.1016/S0012-821X(01)00270-9)
- Barberà, X., Parés, J., Cabrera, L., & Anadón, P. (1994). High-resolution magnetic stratigraphy across the Oligocene-Miocene boundary in an alluvial-lacustrine succession (Ebro Basin, Northeast Spain). *Physics of the Earth and Planetary Interiors*, 85(1), 181–193. [https://doi.org/10.1016/0031-9201\(94\)90016-7](https://doi.org/10.1016/0031-9201(94)90016-7)
- Beltrán Cabrera, F. J., Lanaja del Busto, J. M., & Ríos Aragüés, L. M. (1981). *Mapa Geológico de España--Hoja 468 Albalate del Arzobispo*. Instituto Geológico y Minero de España. Retrieved from <https://info.igme.es/cartografiadigital/geologica/Magna50Hoja.aspx?intranet=false&id=468>
- Bhattacharya, J. P., Copeland, P., Lawton, T. F., & Holbrook, J. (2016). Estimation of source area, river paleo-discharge, paleoslope, and sediment budgets of linked deep-time depositional systems and implications for hydrocarbon potential. *Earth-Science Reviews*, 153, 77–110. <https://doi.org/10.1016/j.earscirev.2015.10.013>
- Bradley, R. W., & Venditti, J. G. (2017). Reevaluating dune scaling relations. *Earth-Science Reviews*, 165, 356–376. <https://doi.org/10.1016/j.earscirev.2016.11.004>
- Buhler, P. B., Fassett, C. L., Head, J. W., & Lamb, M. P. (2014). Timescales of fluvial activity and intermittency in Milna Crater, Mars. *Icarus*, 241, 130–147. <https://doi.org/10.1016/j.icarus.2014.06.028>
- Buj, O., & Gisbert, J. (2010). Influence of pore morphology on the durability of sedimentary building stones from Aragon (Spain) subjected to standard salt decay tests. *Environmental Earth Sciences*, 61(7), 1327–1336. <https://doi.org/10.1007/s12665-010-0451-4>
- Burr, D. M., Enga, M.-T., Williams, R. M. E., Zimbelman, J. R., Howard, A. D., & Brennand, T. A. (2009). Pervasive aqueous paleoflow features in the Aeolis/Zephyria Plana region, Mars. *Icarus*, 200(1), 52–76. <https://doi.org/10.1016/j.icarus.2008.10.014>
- Burr, D. M., Williams, R. M. E., Wendell, K. D., Chojnacki, M., & Emery, J. P. (2010). Inverted fluvial features in the Aeolis/Zephyria Plana region, Mars: Formation mechanism and initial paleodischarge estimates. *Journal of Geophysical Research: Planets*, 115(E7). <https://doi.org/10.1029/2009JE003496>
- Cabrera, L. (1983). *Estratigrafia y Sedimentología de las formaciones lacustres del tránsito Oligoceno-Mioceno del SE de la Cuenca del Ebro*. Departamento de Estratigrafía y Geología Histórica, Universidad de Barcelona. Retrieved from <https://www.tdx.cat/handle/10803/1578#page=7>
- Cabrera, L., Cabrera, M., Gorchs, R., & De Las Heras, F. (2002). Lacustrine basin dynamics and organosulphur compound origin in a carbonate-rich lacustrine system (Late Oligocene Mequinenza Formation, SE Ebro Basin, NE Spain). *Sedimentary Geology*, 148(1), 289–317. [https://doi.org/10.1016/S0037-0738\(01\)00223-8](https://doi.org/10.1016/S0037-0738(01)00223-8)
- Cabrera, L., Colombo, F., & Robles, S. (1985). *Sedimentation and tectonics interrelationships in the Paleogene marginal alluvial systems of the SE Ebro basin: Transition from alluvial to shallow lacustrine environments*. International Association of Sedimentologists, Institut d'Estudis Ilerdencs, Universitat Autònoma de Barcelona.
- Cabrera, L., & Sáez, A. (1987). Coal deposition in carbonate-rich shallow lacustrine systems: The Calaf and Mequinenza sequences (Oligocene, eastern Ebro Basin, NE Spain). *Journal of the Geological Society*, 144(3), 451–461. <https://doi.org/10.1144/gsjgs.144.3.0451>
- Cardenas, B. T., Mohrig, D., & Goudge, T. A. (2018). Fluvial stratigraphy of valley fills at Aeolis Dorsa, Mars: Evidence for base-level fluctuations controlled by a downstream water body. *GSA Bulletin*, 130(3–4), 484–498. <https://doi.org/10.1130/b31567.1>
- Cardenas, B. T., Mohrig, D., Goudge, T. A., Hughes, C. M., Levy, J. S., Swanson, T., et al. (2020). The anatomy of exhumed river-channel belts: Bedform to belt-scale river kinematics of the Ruby Ranch Member, Cretaceous Cedar Mountain Formation, Utah, USA. *Sedimentology*, 67(7), 3655–3682. <https://doi.org/10.1111/sed.12765>
- Costa Mercadal, J. M., Solà Subiranas, J., Olivé Davó, A., Barnolas Cortinas, A., & Robador Moreno, A. (1997). *Mapa Geológico de España--Hoja 442 Caspe*. Instituto Geológico y Minero de España. Retrieved from <https://info.igme.es/cartografiadigital/geologica/Magna50Hoja.aspx?language=es&id=442>

- Craddock, R. A., & Howard, A. D. (2002). The case for rainfall on a warm, wet early Mars. *Journal of Geophysical Research: Planets*, 107(E11), 21-1–21-36. <https://doi.org/10.1029/2001je001505>
- Cuevas Martínez, J. L., Arbués Cazo, P., Cabrera Pérez, L., & Marzo Carpio, M. (2007). Anatomy and architecture of ephemeral, ribbon-like channel-fill deposits of the Caspe Formation (Upper Oligocene to Lower Miocene of the Ebro Basin, Spain). *Sedimentary Processes, Environments and Basins: A Tribute to Peter Friend*, 591–611.
- Cuevas Martínez, J. L., Cabrera Pérez, L., Marcuello, A., Arbués Cazo, P. A. U., Marzo Carpio, M., & Bellmunt, F. (2010). Exhumed channel sandstone networks within fluvial fan deposits from the Oligo-Miocene Caspe Formation, South-east Ebro Basin (North-east Spain). *Sedimentology*, 57(1), 162–189. <https://doi.org/10.1111/j.1365-3091.2009.01096.x>
- Davis, J. M., Grindrod, P. M., Banham, S. G., Warner, N. H., Conway, S. J., Boazman, S. J., & Gupta, S. (2021). A record of syn-tectonic sedimentation revealed by perched alluvial fan deposits in Valles Marineris, Mars. *Geology*. <https://doi.org/10.1130/G48971.1>
- DiBiase, R. A., Limaye, A. B., Scheingross, J. S., Fischer, W. W., & Lamb, M. P. (2013). Deltaic deposits at Aeolis Dorsa: Sedimentary evidence for a standing body of water on the northern plains of Mars. *Journal of Geophysical Research: Planets*, 118(6), 1285–1302. <https://doi.org/10.1002/jgre.20100>
- Dickson, J. L., Lamb, M. P., Williams, R. M. E., Hayden, A. T., & Fischer, W. W. (2021). The global distribution of depositional rivers on early Mars. *Nature Geoscience*. <https://doi.org/10.1130/g48457.1>
- Einstein, H., & Chien, N. (1953). Can the rate of wash load be predicted from the bed-load function? *EOS, Transactions American Geophysical Union*, 34(6), 876–882. <https://doi.org/10.1029/tr034i006p00876>
- Einstein, H. A. (1950). *The bed-load function for sediment transportation in open channel flows* (Vol. 1026). United States Department of Agriculture.
- Engelund, F., & Hansen, E. (1967). *A monograph on sediment transport in alluvial streams* (Vol. 4). Tekniskforlag Skelbreggade.
- Fawdon, P., Gupta, S., Davis, J. M., Warner, N. H., Adler, J. B., Balme, M. R., et al. (2018). The Hypanis Valles delta: The last highstand of a sea on early Mars? *Earth and Planetary Science Letters*, 500, 225–241. <https://doi.org/10.1016/j.epsl.2018.07.040>
- Friend, P., Hirst, J., & Nichols, G. (1986). Sandstone-body structure and river process in the Ebro Basin of Aragón, Spain. *Cuadernos de Geología Iberica*, 10, 9–30.
- Friend, P. F., Slater, M. J., & Williams, R. C. (1979). Vertical and lateral building of river sandstone bodies, Ebro Basin, Spain. *Journal of the Geological Society*, 136(1), 39–46. <https://doi.org/10.1144/gsjgs.136.1.0039>
- Ganti, V., Chu, Z., Lamb, M. P., Nittrouer, J. A., & Parker, G. (2014). Testing morphodynamic controls on the location and frequency of river avulsions on fans versus deltas: Huanghe (Yellow River), China. *Geophysical Research Letters*, 41(22), 7882–7890. <https://doi.org/10.1002/2014GL061918>
- Garcés, M., Cabrera, L., Roca, E., & Gratacós, O. (2008). Comment on “The diachroneity of alluvial-fan lithostratigraphy? A test case from southeastern Ebro basin magnetostratigraphy” by N. Swanson-Hysell and D. L. Barbeau, Jr. *Earth and Planetary Science Letters*, 275(1–2), 181–186. <https://doi.org/10.1016/j.epsl.2008.07.024>
- García-Castellanos, D., & Larrasoaña, J. C. (2015). Quantifying the post-tectonic topographic evolution of closed basins: The Ebro basin (north-east Iberia). *Geology*, 43(8), 663–666. <https://doi.org/10.1130/g36673.1>
- González, A., & Guimerá, J. J. (1993). Sedimentación sintectónica en una cuenca transportada sobre una lámina de cabalgamiento: La cubeta terciaria de Aliaga. *Revista de La Sociedad Geológica de España*, 6(1), 151–165.
- González-Bonarino, G., Colombo, F., & Abascal, L. (2010). Architecture of an Oligocene fluvial ribbon sandstone in the Ebro Basin, North-eastern Spain. *Sedimentology*, 57(3), 845–856.
- Goudge, T. A., Aureli, K. L., Head, J. W., Fassett, C. I., & Mustard, J. F. (2015). Classification and analysis of candidate impact crater-hosted closed-basin lakes on Mars. *Icarus*, 260, 346–367. <https://doi.org/10.1016/j.icarus.2015.07.026>
- Goudge, T. A., Mohrig, D., Cardenas, B. T., Hughes, C. M., & Fassett, C. I. (2018). Stratigraphy and paleohydrology of delta channel deposits, Jezero crater, Mars. *Icarus*, 301, 58–75. <https://doi.org/10.1016/j.icarus.2017.09.034>
- Grotzinger, J. P., & Milliken, R. E. (2012). The sedimentary rock record of Mars: Distribution, origins, and global stratigraphy. *Sedimentary Geology of Mars*, 102, 1–48. <https://doi.org/10.2110/pec.12.102.0001>
- Hajek, E. A., & Heller, P. L. (2012). Flow-depth scaling in alluvial architecture and nonmarine sequence stratigraphy: Example from the castlegate sandstone, Central Utah, U.S.A. *Journal of Sedimentary Research*, 82(2), 121–130. <https://doi.org/10.2110/jsr.2012.8>
- Halevy, I., & Head, J. W. III (2014). Episodic warming of early Mars by punctuated volcanism. *Nature Geoscience*, 7(12), 865–868. <https://doi.org/10.1038/ngeo2293>
- Hayden, A. T., & Lamb, M. P. (2020). Fluvial sinuous ridges of the Morrison formation, USA: Meandering, scarp retreat, and implications for Mars. *Journal of Geophysical Research: Planets*, 125(10). <https://doi.org/10.1029/2020JE006470>
- Hayden, A. T., Lamb, M. P., & Carney, A. J. (2021). Similar curvature-to-width ratios for channels and channel belts: Implications for paleo-hydraulics of fluvial ridges on Mars. *Geology*. <https://doi.org/10.1130/G48370.1>
- Hayden, A. T., Lamb, M. P., Fischer, W. W., Ewing, R. C., McElroy, B., & Williams, R. M. E. (2019). Formation of sinuous ridges by inversion of river-channel belts in Utah, USA, with implications for Mars. *Icarus*, 332, 92–110. <https://doi.org/10.1016/j.icarus.2019.04.019>
- Hayden, A. T., Lamb, M. P., & McElroy, B. J. (2021). Constraining the timespan of fluvial activity from the intermittency of sediment transport on Earth and Mars. *Geophysical Research Letters*. in press. <https://doi.org/10.1029/2021GL092598>
- Heller, P. L., Ratigan, D., Trampush, S., Noda, A., McElroy, B., Drever, J., & Huzurbazar, S. (2015). Origins of bimodal stratigraphy in fluvial deposits: An example from the Morrison formation (Upper Jurassic), Western USA. *Journal of Sedimentary Research*, 85(12), 1466–1477. <https://doi.org/10.2110/jsr.2015.93>
- Hernández Samaniego, A., Ramírez Merino, J. I., & Robador Moreno, A. (2004). *Mapa Geológico de España--Hoja 441 Híjar*. Instituto Geológico y Minero de España. Retrieved from <https://info.igme.es/cartografiadigital/geologica/Magna50Hoja.aspx?intranet=false&id=441>
- Hoke, M. R., Hynke, B. M., & Tucker, G. E. (2011). Formation timescales of large Martian valley networks. *Earth and Planetary Science Letters*, 312(1–2), 1–12. <https://doi.org/10.1016/j.epsl.2011.09.053>
- Howard, A. D., Moore, J. M., & Irwin, R. P. III (2005). An intense terminal epoch of widespread fluvial activity on early Mars: 1. Valley network incision and associated deposits. *Journal of Geophysical Research: Planets*, 110(E12). <https://doi.org/10.1029/2005je002459>
- Hughes, C. M., Cardenas, B. T., Goudge, T. A., & Mohrig, D. (2019). Deltaic deposits indicative of a paleo-coastline at Aeolis Dorsa, Mars. *Icarus*, 317, 442–4534. <https://doi.org/10.1016/j.icarus.2018.08.009>
- Johnson, N. M., Stix, J., Tauxe, L., Cervený, P. F., & Tahirkheli, R. A. (1985). Paleomagnetic chronology, fluvial processes, and tectonic implications of the Siwalik deposits near Chinji village, Pakistan. *The Journal of Geology*, 93(1), 27–40. <https://doi.org/10.1086/628917>
- Jones, M. A., Heller, P. L., Roca, E., Garcés, M., & Cabrera, L. (2004). Time lag of syntectonic sedimentation across an alluvial basin: Theory and example from the Ebro Basin, Spain. *Basin Research*, 16(4), 489–506. <https://doi.org/10.1111/j.1365-2117.2004.00244.x>

- Kite, E. S., Lucas, A., & Fassett, C. I. (2013). Pacing early Mars river activity: Embedded craters in the Aeolis Dorsa region imply river activity spanned $\geq(1-20)$ Myr. *Icarus*, 225(1), 850–855. <https://doi.org/10.1016/j.icarus.2013.03.029>
- Kite, E. S., Howard, A. D., Lucas, A., & Lewis, K. W. (2015). Resolving the era of river-forming climates on Mars using stratigraphic logs of river-deposit dimensions. *Earth and Planetary Science Letters*, 420, 55–65. <https://doi.org/10.1016/j.epsl.2015.03.019>
- Kite, E. S., Howard, A. D., Lucas, A. S., Armstrong, J. C., Aharonson, O., & Lamb, M. P. (2015). Stratigraphy of Aeolis Dorsa, Mars: Stratigraphic context of the great river deposits. *Icarus*, 253(0), 223–242. <https://doi.org/10.1016/j.icarus.2015.03.007>
- Klausen, T. G., Ryseth, A. E., Helland-Hansen, W., Gawthorpe, R., & Laursen, I. (2014). Spatial and temporal changes in geometries of fluvial channel bodies from the Triassic Snadd formation of Offshore Norway. *Journal of Sedimentary Research*, 84(7), 567–585. <https://doi.org/10.2110/jsr.2014.47>
- Kleinbans, M. G. (2005). Flow discharge and sediment transport models for estimating a minimum timescale of hydrological activity and channel and delta formation on Mars. *Journal of Geophysical Research: Planets*, 110(E12). <https://doi.org/10.1029/2005je002521>
- Kleinbans, M. G., van de Kastele, H. E., & Hauber, E. (2010). Palaeoflow reconstruction from fan delta morphology on Mars. *Earth and Planetary Science Letters*, 294(3), 378–392. <https://doi.org/10.1016/j.epsl.2009.11.025>
- Lapôte, M. G. A., & Ielpi, A. (2020). The pace of Fluvial Meanders on Mars and implications for the western delta deposits of Jezero Crater. *AGU Advances*, 1(2), e2019AV000141. <https://doi.org/10.1029/2019av000141>
- Latrubesse, E. M. (2015). Large rivers, megafans and other quaternary avulsive fluvial systems: A potential “who's who” in the geological record. *Earth-Science Reviews*, 146, 1–30. <https://doi.org/10.1016/j.earscirev.2015.03.004>
- Leclair, S. F., & Bridge, J. S. (2001). Quantitative interpretation of sedimentary structures formed by river dunes. *Journal of Sedimentary Research*, 71(5), 713–716. <https://doi.org/10.1306/2DC40962-0E47-11D7-8643000102C1865D>
- Lefort, A., Burr, D. M., Beyer, R. A., & Howard, A. D. (2012). Inverted fluvial features in the Aeolis-Zephyria Plana, western Medusae Fossae formation, Mars: Evidence for post-formation modification. *Journal of Geophysical Research: Planets*, 117(E3). <https://doi.org/10.1029/2011JE004008>
- Lefort, A., Burr, D. M., Nimmo, F., & Jacobsen, R. E. (2015). Channel slope reversal near the Martian dichotomy boundary: Testing tectonic hypotheses. *Geomorphology*, 240, 121–136. <https://doi.org/10.1016/j.geomorph.2014.09.028>
- Leier, A. L., DeCelles, P. G., & Pelletier, J. D. (2005). Mountains, monsoons, and megafans. *Geology*, 33(4), 289–292. <https://doi.org/10.1130/g21228.1>
- Mackin, J. H. (1948). Concept of the Graded River. *GSA Bulletin*, 59(5), 463–512. [https://doi.org/10.1130/0016-7606\(1948\)59\[463:cotgr\]2.0.co;2](https://doi.org/10.1130/0016-7606(1948)59[463:cotgr]2.0.co;2)
- Mohrig, D., Heller, P. L., Paola, C., & Lyons, W. J. (2000). Interpreting avulsion process from ancient alluvial sequences: Guadalupe-Matarranya system (northern Spain) and Wasatch Formation (western Colorado). *The Geological Society of America Bulletin*, 112(12), 1787–1803. [https://doi.org/10.1130/0016-7606\(2000\)112<1787:iapfaa>2.0.co;2](https://doi.org/10.1130/0016-7606(2000)112<1787:iapfaa>2.0.co;2)
- Moore, J. M., Howard, A. D., Dietrich, W. E., & Schenk, P. M. (2003). Martian layered fluvial deposits: Implications for Noachian climate scenarios. *Geophysical Research Letters*, 30(24). <https://doi.org/10.1029/2003GL019002>
- Morgan, A. M., Howard, A. D., Hobley, D. E. J., Moore, J. M., Dietrich, W. E., Williams, R. M. E., et al. (2014). Sedimentology and climatic environment of alluvial fans in the martian Saheki crater and a comparison with terrestrial fans in the Atacama Desert. *Icarus*, 229, 131–156. <https://doi.org/10.1016/j.icarus.2013.11.007>
- Navarro Juli, J. J., Portero García, G., & Robador Moreno, A. (1994). *Mapa Geológico de España--Hoja 469 Alcañiz*. Instituto Geológico y Minero de España. Retrieved from <https://info.igme.es/cartografiadigital/geologica/Magna50Hoja.aspx?intranet=false&id=469>
- Nichols, G. J., & Fisher, J. A. (2007). Processes, facies and architecture of fluvial distributary system deposits. *Sedimentary Geology*, 195(1), 75–90. <https://doi.org/10.1016/j.sedgeo.2006.07.004>
- Orofino, V., Alemanno, G., Di Achille, G., & Mancarella, F. (2018). Estimate of the water flow duration in large Martian fluvial systems. *Planetary and Space Science*, 163, 83–96. <https://doi.org/10.1016/j.pss.2018.06.001>
- Pain, C., Clarke, J., & Thomas, M. (2007). Inversion of relief on Mars. *Icarus*, 190(2), 478–491. <https://doi.org/10.1016/j.icarus.2007.03.017>
- Pain, C. F., & Ollier, C. D. (1995). Inversion of relief—a component of landscape evolution. *Geomorphology*, 12(2), 151–165. [https://doi.org/10.1016/0169-555x\(94\)00084-5](https://doi.org/10.1016/0169-555x(94)00084-5)
- Palumbo, A. M., Head, J. W., & Wilson, L. (2020). Rainfall on Noachian Mars: Nature, timing, and influence on geologic processes and climate history. *Icarus*, 347, 113782. <https://doi.org/10.1016/j.icarus.2020.113782>
- Palumbo, A. M., Head, J. W., & Wordsworth, R. D. (2018). Late Noachian Icy Highlands climate model: Exploring the possibility of transient melting and fluvial/lacustrine activity through peak annual and seasonal temperatures. *Icarus*, 300, 261–286. <https://doi.org/10.1016/j.icarus.2017.09.007>
- Paola, C., & Borgman, L. (1991). Reconstructing random topography from preserved stratification. *Sedimentology*, 38(4), 553–565. <https://doi.org/10.1111/j.1365-3091.1991.tb01008.x>
- Paola, C., Heller, P. L., & Angevine, C. L. (1992). The large-scale dynamics of grain-size variation in alluvial basins. I: Theory. *Basin Research*, 4(2), 73–90. <https://doi.org/10.1111/j.1365-2117.1992.tb00145.x>
- Parker, G., Wilcock, P. R., Paola, C., Dietrich, W. E., & Pitlick, J. (2007). Physical basis for quasi-universal relations describing bankfull hydraulic geometry of single-thread gravel bed rivers. *Journal of Geophysical Research: Earth Surface*, 112(F4). <https://doi.org/10.1029/2006jf000549>
- Pérez-Rivarés, J., Crespo, M. G., Abad, M. C. A., & Tirapu, G. P. (2004). Magnetostratigraphy of the Miocene continental deposits of the Montes de Castejón (central Ebro basin, Spain): Geochronological and paleoenvironmental implications. *Geológica Acta*, 2(3), 221–234.
- Petkovsek, G. (2019). A review of Ackers and White sediment transport predictor. Presented at the *Proceedings of the Institution of Civil Engineers-water Management* (pp. 1–13). Thomas Telford Ltd.
- Pollack, J. B., Kasting, J. F., Richardson, S. M., & Poliakov, K. (1987). The case for a wet, warm climate on early Mars. *Icarus*, 71(2), 203–224. [https://doi.org/10.1016/0019-1035\(87\)90147-3](https://doi.org/10.1016/0019-1035(87)90147-3)
- Riba, O., Villena, J., & Quirantes, J. (1967). *Nota preliminar sobre la sedimentacion en paleocanales terciarios de la zona de Caspe-Chiprana (Provincia de Zaragoza)*.
- Robinson, J. W., & McCabe, P. J. (1997). Sandstone-body and shale-body dimensions in a braided fluvial system: Salt Wash Sandstone Member (Morrison Formation), Garfield County, Utah. *AAPG Bulletin*, 81(8), 1267–1291. <https://doi.org/10.1306/522B4DD9-1727-11D7-8645000102C1865D>
- Sadler, P. M. (1981). Sediment accumulation rates and the completeness of stratigraphic sections. *The Journal of Geology*, 569–584. <https://doi.org/10.1086/628623>
- Sadler, P. M., & Jerolmack, D. J. (2015). Scaling laws for aggradation, denudation and progradation rates: The case for time-scale invariance at sediment sources and sinks. *Geological Society, London, Special Publications*, 404(1), 69–88. <https://doi.org/10.1144/sp404.7>
- Schumm, S. A. (1972). *Fluvial paleochannels*. Special Publication - Society of Economic Paleontologists and Mineralogists.
- Segura, T. L., Toon, O. B., Colaprete, A., & Zahnle, K. (2002). Environmental effects of large impacts on Mars. *Science*, 298(5600), 1977–1980. <https://doi.org/10.1126/science.1073586>

- Slingerland, R., & Smith, N. D. (2004). River avulsions and their deposits. *Annual Review of Earth and Planetary Sciences*, 32, 257–285. <https://doi.org/10.1146/annurev.earth.32.101802.120201>
- Stack, K. M., Grotzinger, J. P., Lamb, M. P., Gupta, S., Rubin, D. M., Kah, L. C., et al. (2019). Evidence for plunging river plume deposits in the Pahrump Hills member of the Murray formation, Gale crater, Mars. *Sedimentology*, 66(5), 1768–1802. <https://doi.org/10.1111/sed.12558>
- Stokes, W. L. (1953). *Primary sedimentary trend indicators as applied to ore finding in the Carrizo Mountains, Arizona and New Mexico; Part 1, Technical report for April 1, 1952 to March 31, 1953*. U. S. Atomic Energy Commission, Report. Retrieved from <https://cdsproxy.library.caltech.edu/login?url=http://search.ebscohost.com/login.aspx?direct=true&db=geh&AN=1959-029637&site=eds-live&scope=site>
- Stucky de Quay, G., Goudge, T. A., & Fassett, C. I. (2020). Precipitation and aridity constraints from paleolakes on early Mars. *Geology*. <https://doi.org/10.1130/g47886.1>
- Swanson-Hysell, N., & Barbeau, D. L. (2007). The diachroneity of alluvial-fan lithostratigraphy? A test case from southeastern Ebro basin magnetostratigraphy. *Earth and Planetary Science Letters*, 262(3–4), 343–362. <https://doi.org/10.1016/j.epsl.2007.07.003>
- Swanson-Hysell, N., & Barbeau, D. L. (2008). Reply to Garcés et al. comment on ‘The diachroneity of alluvial-fan lithostratigraphy? A test case from southeastern Ebro Basin magnetostratigraphy’ *Earth and Planetary Science Letters*, 275(1–2), 187–192. <https://doi.org/10.1016/j.epsl.2008.07.018>
- Trampush, S. M., Huzurbazar, S., & McElroy, B. J. (2014). Empirical assessment of theory for bankfull characteristics of alluvial channels. *Water Resources Research*, 50(12), 9211–9220. <https://doi.org/10.1002/2014WR015597>
- Valero, L., Garcés, M., Cabrera, L., Costa, E., & Sáez, A. (2014). 20 Myr of eccentricity paced lacustrine cycles in the Cenozoic Ebro Basin. *Earth and Planetary Science Letters*, 408, 183–193. <https://doi.org/10.1016/j.epsl.2014.10.007>
- Van Den Hurk, A., Navarro Juli, J. J., Pascual Muñoz, H., Barnolas Cortinas, A., & Robador Moreno, A. (1997). *Mapa Geológico de España--Hoja 443 Fabara*. Instituto Geológico y Minero de España. Retrieved from <https://info.igme.es/cartografiadigital/geologica/Magna50Hoja.aspx>
- Williams, R. C. (1975). *Fluvial deposits of Oligo-Miocene Age in the southern Ebro basin*. University of Cambridge.
- Williams, R. M. E., Grotzinger, J. P., Dietrich, W., Gupta, S., Sumner, D., Wiens, R., et al. (2013). Martian fluvial conglomerates at Gale crater. *Science*, 340(6136), 1068–1072.
- Williams, R. M. E., Irwin, R. P., & Zimbelman, J. R. (2009). Evaluation of paleohydrologic models for terrestrial inverted channels: Implications for application to martian sinuous ridges. *Geomorphology*, 107(3–4), 300–315. <https://doi.org/10.1016/j.geomorph.2008.12.015>
- Wordsworth, R., Ehlmann, B., Forget, F., Haberle, R., Head, J., & Kerber, L. (2018). Healthy debate on early Mars. *Nature Geoscience*, 11(12), 888. <https://doi.org/10.1038/s41561-018-0267-5>
- Zaki, A., Pain, C., Edgett, K. S., & Castellort, S. (2021). Global inventory of fluvial ridges on Earth and lessons applicable to Mars. *Earth-Science Reviews*, 216, 103561. <https://doi.org/10.1016/j.earscirev.2021.103561>